International Journal of Earth Sciences (2018) 107:1955–1974
https://doi.org/10.1007/s00531-017-1581-7

ORIGINAL PAPER

Early cretaceous lower crustal reworking in NE China: insights from geochronology and geochemistry of felsic igneous rocks from the Great Xing'an range

Yinglei Li[1] · Huichuan Liu[2] · Pengpeng Huangfu[3] · Hongyun He[1] · Yongzheng Liu[1]

Received: 13 August 2017 / Accepted: 21 December 2017 / Published online: 4 January 2018

Abstract

This paper presents new zircon LA-ICP-MS U–Pb ages and whole-rock geochemical data for two granitic plutons and rhyolites of the Baiyingaolao Formation in the western Xing'an range (NE China). The two syenogranite granitic plutons yield identical zircon U–Pb age of 142 ± 1 Ma, and the Baiyingaolao rhyolites yield zircon U–Pb age of 138 ± 2 Ma. The granites contain some hornblendes, and show low Zr and Zr + Nb + Ce + Y contents, and low A/CNK (0.98–1.11), $Mg^{\#}$ (6–55), and FeOT/MgO values. Rhyolite samples show similar geochemical characteristics with A/CNK of 0.99–1.10 and $Mg^{\#}$ of 14–21. In combination with the high K_2O contents (4.43–5.61 wt%) and negative correlations between P_2O_5 and SiO_2, both the granites and rhyolites were classified as high-K calc-alkaline I-type granitoids. All samples give high zirconium saturation temperature of 794–964 °C with few initially inherited zircons, and belong to high-temperature I-type granitoids. They were generated by dehydration melting of biotite/muscovite from sub-alkaline meta-basalts in lower crust depth, leaving garnet, amphibole, and plagioclase as the major residual minerals. The syenogranites and rhyolites are likely formed in Mongol–Okhotsk oceanic subduction setting. Incorporating other lower crust-originated felsic rocks in Erguna and Xing'an massifs and Songliao basin, it is argued that lower crustal reworking is pronounced in NE China during Early Cretaceous.

Keywords Lower crustal reworking · I-type granitoids · Back-arc extension · NE China · Mongol–Okhotsk Ocean

Introduction

Crustal growth and reworking are two major geodynamic processes for Phanerozoic continental crust evolution (Heilimo et al. 2014; Kemp et al. 2007b; Sengor et al. 1993; Spencer et al. 2014). Crustal growth means extracting material from the upper mantle to the earth's surface (Albarede 1998) and is generally ascribed to vertical addition of mafic magma underplating at the crust–mantle interface (in intraplate settings) and lateral accretion of arc complexes at convergent margins (Kemp et al. 2009; Rapp et al. 2003; Rudnick 1995; Rudnick and Fountain 1995; Tang et al. 2012). Crustal reworking means partial melting of the lower, middle, and upper crust, and transferring magma to the upper crust, causing the chemical differentiation of the continental crust (Sawyer 1998). Crustal reworking may occur in various tectonic environments, including continental arc/back-arc basin (Heilimo et al. 2014; Yang et al. 2016), syn-/post-collision (Spencer et al. 2014; Xiong et al. 2014; Zeitler et al. 2001), within plate (Jayananda et al. 2006), and even mantle plume-related settings (Shellnutt and Zhou 2007).

The Central Asian Orogenic Belt (CAOB; Fig. 1a) is regarded as the most pronounced site of Phanerozoic crustal growth and reworking in the world (Guo et al. 2010; Jahn et al. 2000a, b, 2004; Safonova 2017; Tang et al. 2012; Wu et al. 2003). NE China is located in the eastern segment of the CAOB (Fig. 1a), and has been jointly

Electronic supplementary material The online version of this article (https://doi.org/10.1007/s00531-017-1581-7) contains supplementary material, which is available to authorized users.

✉ Huichuan Liu
liuhuichuan1986@126.com

[1] Inner Mongolia Key Laboratory of Magmatic Mineralization and Ore-Prospecting, Geological Survey Institute of Inner Mongolia, Hohhot 010020, China

[2] Present Address: School of Earth Science and Engineering, Sun Yat-Sen University, Guangzhou 510275, China

[3] Key Laboratory of Computational Geodynamics, College of Earth Sciences, University of Chinese Academy of Sciences, Beijing 100049, China

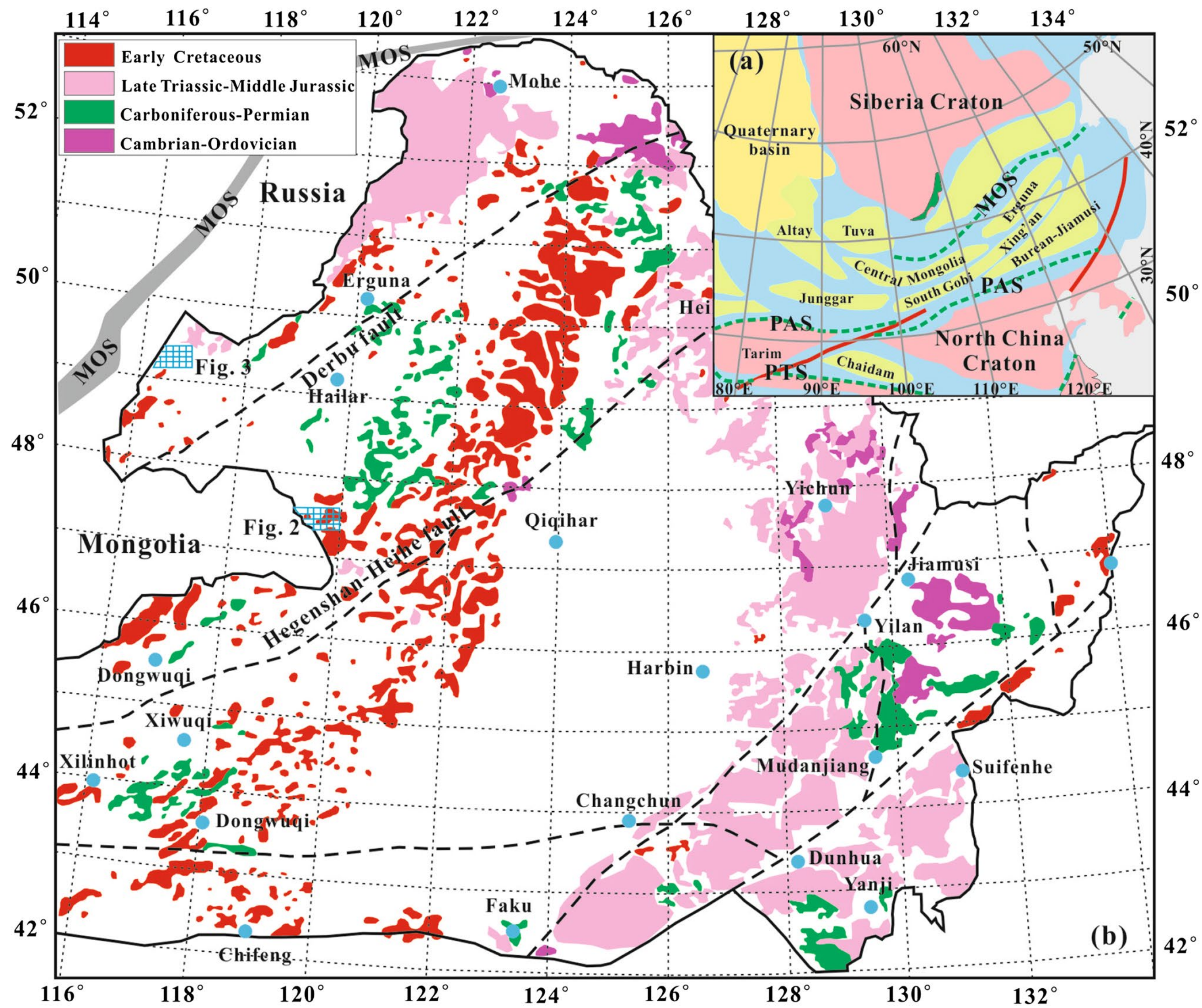

Fig. 1 **a** Tectonic outline of Northeast Asia (modified after Tang et al. 2016) and **b** simplified geological map of NE China (after Li et al. 2017a and; Wu et al. 2011). *MOS* Mongol–Okhotsk suture, *PAS* Paleo-Asian suture, *PTS* Paleo-Tethys suture

influenced by the Paleo-Asian Ocean closure, the Paleo-Pacific, and Mongol–Okhotsk subductions (Chen et al. 2017; Kelty et al. 2008; Liu et al. 2017; Tang et al. 2016; Wang et al. 2015a). The previous studies have shown that NE China is composed of mainly subduction–accretion complexes, intruded by vast plutons of mainly magmatic arc origin and covered in places by their volcanic derivatives, and thus, the Phanerozoic crustal growth in NE China is dominated by lateral accretion (Chen et al. 2017; Kelty et al. 2008; Liu et al. 2017; Tang et al. 2016; Wang et al. 2015c). However, less attention has been paid to the Phanerozoic crustal reworking in NE China (Safonova 2017). Whether there occurred Phanerozoic crustal reworking in NE China, and the timing and location are still pending problems.

Felsic magmatism represents a major contribution to continental crust and plays an important role in evaluating crustal growth/reworking, and addressing thermal and geodynamic evolution (Hawkesworth and Kemp 2006; Kemp et al. 2007a; Rudnick 1995; Rudnick and Fountain 1995). Phanerozoic felsic rocks (mainly granites and rhyolites) are widely distributed in NE China. In this study, we collected Early Cretaceous rhyolite and syenogranite samples from the western Xing'an range (Fig. 1b; NE China). Then, we conducted zircon U–Pb dating as well as the whole-rock geochemical analyses for these Early Cretaceous felsic rocks, to unravel their origin and evaluate the Early Cretaceous crustal reworking in NE China.

Regional geological background and sample descriptions

Siberian, Tarim, and North China cratons collided during late Paleozoic-to-early Mesozoic, building up the CAOB through a gigantic accretionary orogeny associated with the Paleo–Asian Ocean closure (Fig. 1a; Long et al. 2007; Meng et al. 2010; Pei et al. 2016; Xiao et al. 2013, 2003). NE China is located in the eastern section of the CAOB, and consists of the Khanka, Jiamusi, Songnen–Zhangguangcai Range, Xing'an, and Erguna massifs (Fig. 1a, Fritzell et al. 2016; Wang et al. 2006, 2016). These massifs were separated from the Siberia craton to the north by the Mongol–Okhotsk suture and the North China craton to the south by the Solonker suture (Fig. 1a). The Paleo-Asian Ocean, Paleo-Pacific, and Mongol–Okhotsk subductions (Chen et al. 2017; Kelty et al. 2008; Liu et al. 2017; Tang et al. 2016; Wang et al. 2015c) have jointly shaped this area at different time. The Paleo-Asian ocean was closed along the Solonker suture possibly during Early Permian-to-Late Triassic (Wang et al. 2015c; Yang et al. 2017; Zhou et al. 2017).

Our samples were collected from the Erguna and Xing'an massifs (Fig. 1b). The Erguna and Xing'an massifs located between the Mongol–Okhotsk suture and Hegenshan–Heihe fault (Fig. 1b). The Erguna massif is connected with the central Mongolia massif and the Xing'an massif is connected with the South Gobi massif. Their basement consists of Precambrian metamorphic supracrustal rocks and intrusions (IMBGMR 1991). Multiple middle Mesozoic volcanic rocks and clastic sedimentary rocks are widespread in these two massfis, including the Tamulangou (J_2tm), Manketouebo (J_3mk), Manitu (K_3mn), Baiyingaolao (K_1b), and Meiletu (K_1m) formations (Figs. 2, 3; Dong et al. 2014; Ji et al. 2016; Li et al. 2015; Sun et al. 2011). Late Paleozoic-to-Mesozoic granitoids also occur in the Erguna and Xing'an massifs with an NE–SW orientation, parallel to the Mongol–Okhotsk suture (Sun et al. 2001; Zhao et al. 2014).

Fifteen medium-grained syenogranite samples were collected from 10 km south of the Tuoliela village (in the lower-left corner of Fig. 2). They are brick-colored red and contained 60–65% alkali feldspar, 10–15% plagioclase, 20–25% quartz, and ~5% biotite (Supplemental file 1).

Seven fine-grained syenogranite samples were collected from 10 km southwest of the Wuertu village (in the upper-left corner of Fig. 2). They exhibit a porphyritic texture in which perthite and xenomorphic quartz are embedded in a fine-grained groundmass. The phenocryst is composed of 5–8% perthite and 2–5% quartz. The groundmass is composed of 40–50% perthite, 10–15% plagioclase, ~20% quartz, and minor biotite (Supplemental file 1).

Four rhyolite samples were collected from the Baiyingaolao Formation in 3 km north of the Hanwulan volcanic vent (in the upper-right corner of Fig. 3). The Baiyingaolao Formation (K_1b) unconformably overlies on the Manitu Formation Manitu (K_3mn) and is unconformably overlian by the Meiletu formation (K_1m). The Baiyingaolao Formation is composed mainly of rhyolites and rhyolitic tuffs, with minor trachy dacites. The four rhyolite samples is grayish yellow in color (Supplemental file 1), displaying a porphyritic texture with a groundmass of a glassy or microcrystalline texture. The phenocrysts (~5%) are alkali feldspar (~2%) and plagioclase (~3%).

Analytical methods

Zircon grains were extracted using the conventional heavy liquid and magnetic techniques, and were mounted in epoxy, then polished, and coated with gold for cathodoluminescence (CL) imaging at Guangdong Provincial Key Laboratory of Mineral Resources and Geological Processes, Sun Yat-sen University, Guangzhou, China.

Zircon U-Pb dating and trace element analyses were conducted using a laser ablation–inductively coupled plasma–mass spectrometry (LA-ICP-MS) at Tianjin Geological Survey Center (China). The zircon standards 91,500 and GJ were used to calibrate the U–Th–Pb ratios. The spot size for data collection was 30 μm. The errors for individual U–Pb analyses are presented with 1σ error and uncertainties in grouped ages are quoted at 95% level (1σ). Off-line inspection and integration of background and analysis signals, and time-drift correction and quantitative calibration for trace element analyses and U–Pb dating were performed using ICP-MS DataCal (Liu et al. 2010). Further detailed descriptions of the instrumentation and analytical procedure for the LA-ICP-MS zircon U–Pb and trace element technique are similar to those described by Yuan et al. (2004).

Whole-rock samples for geochemistry were crushed to 200 mesh using an agate mill for elemental and Sr–Nd isotopic analyses. The major oxides were analyzed by a wavelength X-ray fluorescence spectrometry at Tianjin Geological Survey Center (China). Trace element analyses were performed at the Tianjin Geological Survey Center by a X Series II ICP-MS. Detailed sample preparation and analytical procedure followed Li et al. (2002).

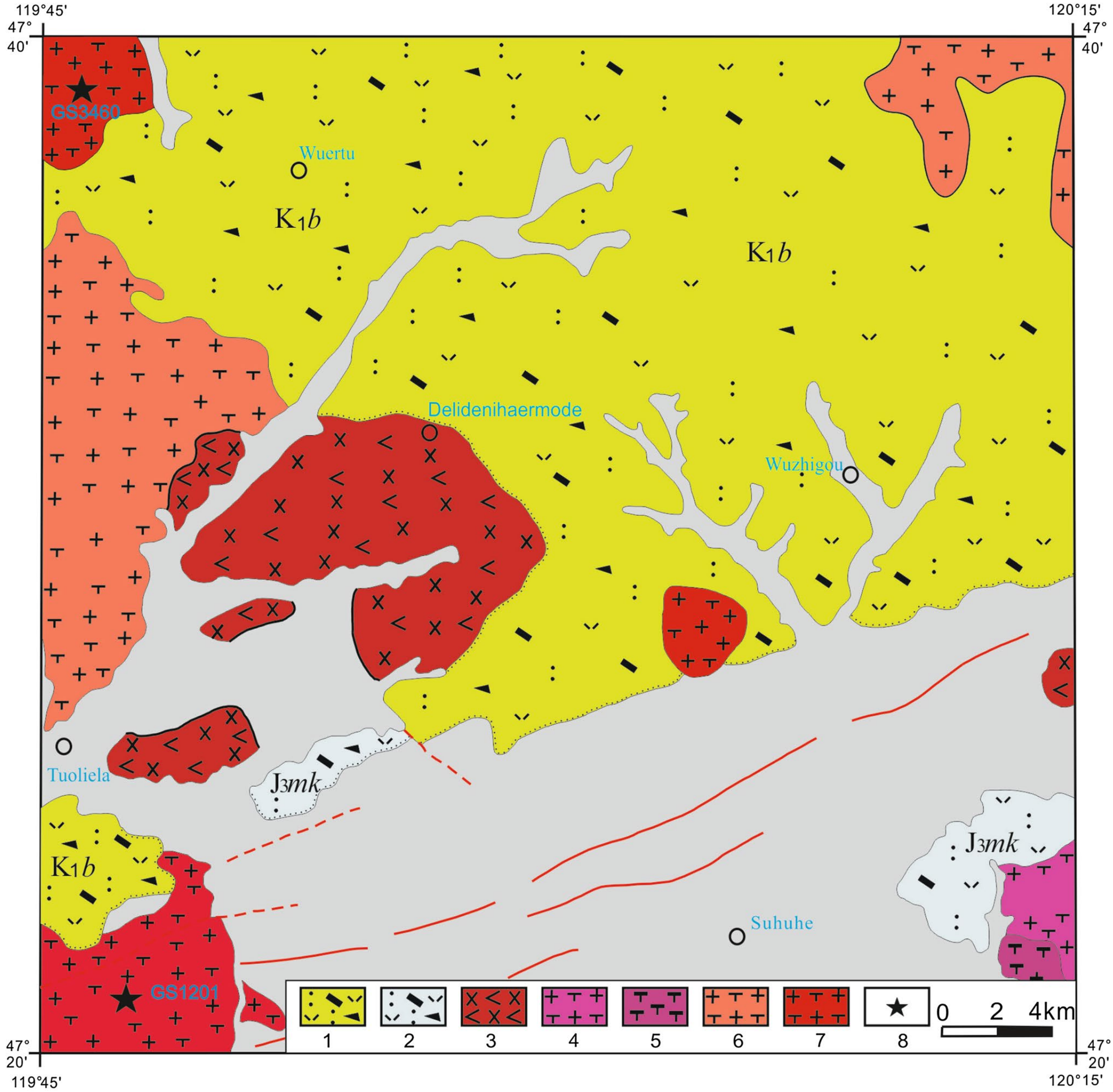

Fig. 2 Geological map showing the stratigraphic and igneous components of the Delidenihaermode area (modified from IMBGMR 1991). 1—Baiyingaolao formation, 2—Manketouebo formation, 3—Gabbro, 4—Middle Triassic granite, 5—Late Triassic granite, 6—Middle Jurassic granite, 7—Cretaceous granite, and 8—Sample location

Geochronological and geochemical characteristics

Geochronology

Fine- and medium-grained syenogranite

Samples GS1201 (medium-grained syenogranite) from the Tuoliela area and GS5892 (fine-grained syenogranite) from the Wuertu area were collected for LA-ICP-MS zircon U–Pb dating (Table 1; Fig. 4). Zircon grains from sample GS1201 were subhedral-to-euhedral, transparent-to-colorless, and stubby-to-elongate in shape with lengths of 70–200 µm and widths of 50–100 µm (Fig. 4d). Zircon grains from sample GS3460 were subhedral and fragmentary, transparent to colorless, and stubby in shape with lengths of 70–100 µm and widths of 50–90 µm (Fig. 4e). Backscatter electron (BSE) and cathodoluminescence (CL)

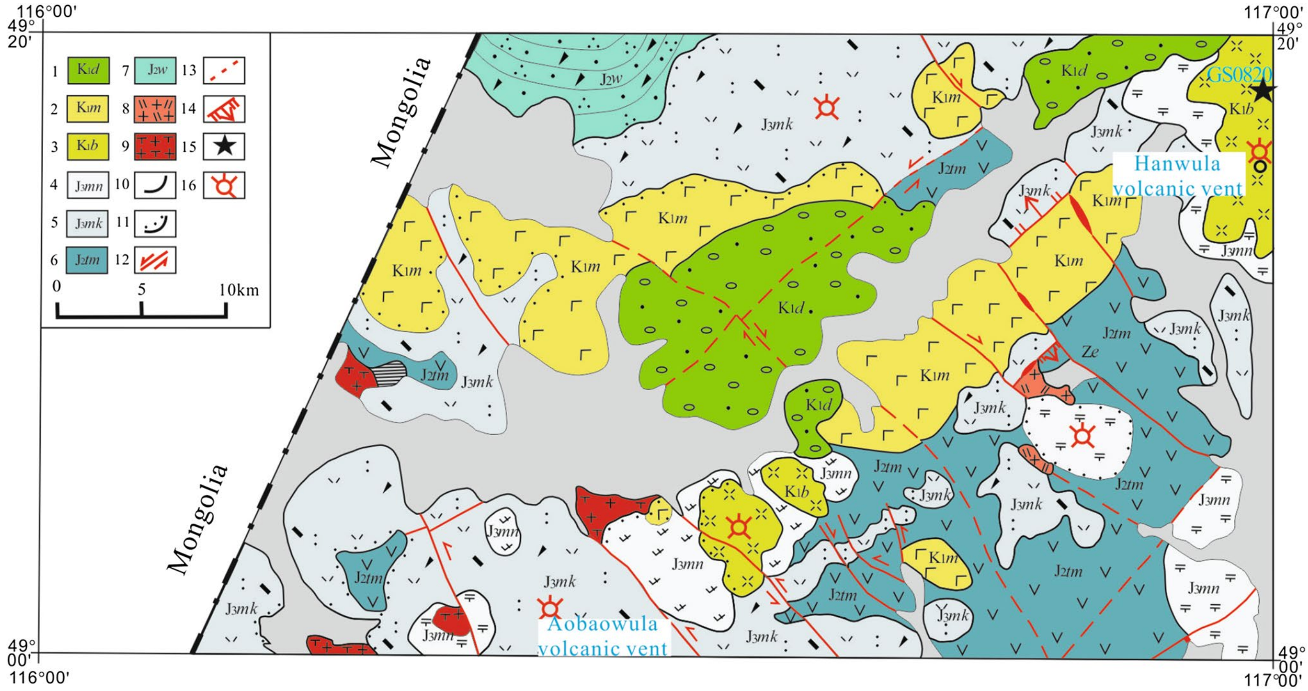

Fig. 3 Geological map showing the stratigraphic and igneous components of the Aobaowula area (modified from Li et al. 2017b). 1—Damoguaihe formation, 2—Meiletu formation, 3—Baiyingaolao formation, 4—Manitu formation, 5—Manketouebo formation, 6—Tamulangou formation, 7—Wanbao formation, 8—Late Jurassic granite, 9—Permian granite, 10—Stratigraphic boundary, 11—Stratigraphic unconformity, 12—Strike slip fault, 13—Inferred fault, 14—Normal fault, 15—Sample location, and 16—Volcanic vent

images of all grains display well-preserved growth zones, with unperturbed oscillatory zoning, typical of igneous zircon (Hanchar and Miller 1993). Zircon U-Pb dating results are listed in Table 1 and presented on Concordia plots in Fig. 4a, b.

Twenty-four analyses were performed on 24 zircons from samples GS1201. Except one spot (GS1201.20) with Th/U = 0.06, these analyses documented Th/U ratios ranging from 0.3 to 1.6, reflective of an igneous origin. The 24 analyses show $^{206}Pb/^{238}U$ apparent ages ranging from 139 to 144 Ma and yield a weighted mean $^{206}Pb/^{238}U$ age of 142 ± 1 Ma [mean square of weighted deviates (MSWD) = 0.8, n = 24; Fig. 4a]. This age (142 Ma) is interpreted as the crystalline age of the medium-grained syenogranite.

Twenty analyses were performed on 20 zircon grains from syenogranite sample GS3460. Except one spot (GS3460.16) with Th/U = 0.06, these analyses document Th/U ratios varying from 0.3 to 1.3, which are consistent with an igneous origin (Fig. 4b). One analysis (GS3460.19) yields $^{206}Pb/^{238}U$ age of 172 ± 2 Ma, interpreted as the result of inheritance. The remaining 19 analyses form a homogenous cluster and yield a weighted mean $^{206}Pb/^{238}U$ age of 142 ± 1 Ma (MSWD = 1.4, n = 19, Fig. 4b). This age (142 Ma) is interpreted as the crystalline age of the fine-grained syenogranite.

Rhyolite

Sample GS0820 (rhyolite) from the Hanwula area were collected for LA-ICP-MS zircon U–Pb dating. Zircon grains were stubby in shape with lengths of 70–150 μm and widths of 50–90 μm. Cathodoluminescence (CL) images of all grains display well-preserved subhedral-to-euhedral growth zones, typical of igneous zircon (Fig. 4f; Hanchar and Miller 1993). Zircon U–Pb dating results are listed in Table 1 and presented on Concordia plots in Fig. 4c.

Twenty-two analyses were performed on 22 zircon grains from rhyolite sample GS0820. These analyses document high Th/U ratios varying from 1.1 to 3.5, consistent with an igneous origin. Except one analysis (GS0820.12) showing an inherited $^{206}Pb/^{238}U$ age of 155 Ma, they yield $^{206}Pb/^{238}U$ apparent ages between 126 Ma and 143 Ma, and a weighted mean age of 138 ± 2 Ma with MSWD = 4.9 (n = 21, Fig. 4c). This age (138 Ma) is interpreted as the eruption age of the rhyolite.

Geochemical characteristics

Fine- and medium-grained syenogranites

The fine- and medium-grained syenogranites show similar geochemical characteristics (Table 2), and were plotted in

Table 1 LA-ICP-MS zircon U-Pb dating results for the Tuoliela syenogranite (GS1201), Wuertu syenogranite (GS3460), and Hanwula rhyolite (GS0820) in Erguna and Xing'an massifs

Spot	Th/U	Isotopic ratios						Isotopic ages			
		$^{206}Pb/^{238}U$	1σ	$^{207}Pb/^{235}U$	1σ	$^{207}Pb/^{206}Pb$	1σ	$^{206}Pb/^{238}U$	1σ	$^{207}Pb/^{235}U$	1σ
GS1201											
GS1201.1	1.02	0.02252	0.00026	0.15308	0.00602	0.04929	0.00185	143.6	1.6	144.6	5.7
GS1201.2	1.19	0.02188	0.00029	0.14840	0.01790	0.04918	0.00610	139.5	1.9	140.5	16.9
GS1201.3	0.63	0.02252	0.00025	0.15578	0.00573	0.05016	0.00175	143.6	1.6	147.0	5.4
GS1201.4	0.98	0.02252	0.00026	0.15587	0.01101	0.05021	0.00359	143.5	1.7	147.1	10.4
GS1201.5	1.24	0.02214	0.00025	0.14924	0.00790	0.04888	0.00256	141.2	1.6	141.2	7.5
GS1201.6	1.10	0.02244	0.00029	0.15319	0.00521	0.04952	0.00175	143.0	1.8	144.7	4.9
GS1201.7	1.03	0.02244	0.00031	0.15120	0.01408	0.04886	0.00451	143.1	2.0	143.0	13.3
GS1201.8	1.00	0.02210	0.00028	0.15227	0.00772	0.04998	0.00245	140.9	1.8	143.9	7.3
GS1201.9	1.59	0.02200	0.00025	0.14760	0.00662	0.04866	0.00220	140.3	1.6	139.8	6.3
GS1201.10	0.89	0.02253	0.00026	0.15463	0.00377	0.04978	0.00111	143.6	1.7	146.0	3.6
GS1201.11	1.10	0.02255	0.00025	0.15706	0.00758	0.05052	0.00246	143.8	1.6	148.1	7.1
GS1201.12	0.77	0.02235	0.00027	0.15461	0.00442	0.05016	0.00136	142.5	1.7	146.0	4.2
GS1201.13	1.44	0.02218	0.00024	0.15077	0.00391	0.04930	0.00124	141.4	1.6	142.6	3.7
GS1201.14	1.38	0.02179	0.00028	0.15197	0.00625	0.05058	0.00209	139.0	1.8	143.6	5.9
GS1201.15	0.88	0.02219	0.00031	0.15005	0.01203	0.04905	0.00388	141.5	1.9	142.0	11.4
GS1201.16	0.95	0.02255	0.00029	0.15123	0.00321	0.04863	0.00095	143.8	1.8	143.0	3.0
GS1201.17	0.32	0.02229	0.00026	0.15674	0.00369	0.05100	0.00112	142.1	1.6	147.8	3.5
GS1201.18	1.48	0.02203	0.00026	0.15154	0.00566	0.04990	0.00183	140.5	1.7	143.3	5.4
GS1201.19	0.83	0.02259	0.00027	0.15246	0.01062	0.04896	0.00342	144.0	1.7	144.1	10.0
GS1201.20	0.06	0.02217	0.00032	0.15453	0.02043	0.05056	0.00707	141.3	2.1	145.9	19.3
GS1201.21	0.76	0.02233	0.00027	0.15251	0.01283	0.04954	0.00417	142.3	1.7	144.1	12.1
GS1201.22	0.65	0.02209	0.00025	0.15014	0.01135	0.04929	0.00375	140.8	1.6	142.0	10.7
GS1201.23	0.53	0.02262	0.00026	0.15447	0.01106	0.04952	0.00354	144.2	1.6	145.9	10.4
GS1201.24	0.81	0.02204	0.00023	0.14900	0.00574	0.04903	0.00187	140.5	1.5	141.0	5.4
GS3460											
GS3460.1	1.04	0.02268	0.00026	0.15624	0.00540	0.04995	0.00170	144.6	1.7	147.4	5.1
GS3460.2	0.94	0.02231	0.00024	0.15367	0.00682	0.04996	0.00216	142.2	1.6	145.1	6.4
GS3460.3	0.98	0.02202	0.00023	0.15069	0.00424	0.04963	0.00135	140.4	1.5	142.5	4.0
GS3460.4	0.89	0.02179	0.00024	0.15002	0.00291	0.04993	0.00084	139.0	1.5	141.9	2.8
GS3460.5	1.33	0.02217	0.00023	0.15185	0.00491	0.04967	0.00157	141.4	1.5	143.5	4.6
GS3460.6	0.84	0.02212	0.00023	0.15410	0.00290	0.05052	0.00085	141.0	1.5	145.5	2.7
GS3460.7	1.03	0.02253	0.00026	0.15374	0.01126	0.04950	0.00340	143.6	1.7	145.2	10.6
GS3460.8	1.05	0.02183	0.00026	0.15035	0.01564	0.04995	0.00530	139.2	1.7	142.2	14.8
GS3460.9	0.75	0.02236	0.00025	0.15396	0.01037	0.04994	0.00331	142.5	1.6	145.4	9.8
GS3460.10	1.05	0.02241	0.00025	0.15695	0.00498	0.05080	0.00155	142.9	1.6	148.0	4.7
GS3460.11	0.77	0.02170	0.00026	0.15023	0.01491	0.05022	0.00460	138.4	1.7	142.1	14.1
GS3460.12	0.78	0.02243	0.00025	0.15269	0.00805	0.04938	0.00257	143.0	1.6	144.3	7.6
GS3460.13	1.09	0.02210	0.00031	0.15040	0.00309	0.04937	0.00088	140.9	2.0	142.3	2.9
GS3460.14	0.84	0.02261	0.00030	0.15405	0.00913	0.04942	0.00278	144.1	1.9	145.5	8.6
GS3460.15	0.32	0.02254	0.00029	0.15224	0.01527	0.04899	0.00486	143.7	1.8	143.9	14.4
GS3460.16	0.06	0.02250	0.00026	0.15504	0.00941	0.04996	0.00300	143.5	1.7	146.4	8.9
GS3460.17	0.81	0.02175	0.00024	0.15035	0.00680	0.05014	0.00217	138.7	1.5	142.2	6.4
GS3460.18	1.10	0.02257	0.00029	0.15337	0.01334	0.04929	0.00426	143.9	1.9	144.9	12.6
GS3460.19	0.90	0.02711	0.00037	0.18641	0.00421	0.04988	0.00097	172.4	2.4	173.6	3.9
GS3460.20	0.77	0.02243	0.00030	0.15741	0.00703	0.05090	0.00196	143.0	1.9	148.4	6.6
GS08-20											
GS0820.1	1.81	0.16993	0.01381	0.02200	0.00018	0.05644	0.00458	140.3	1.2	159.4	8.2

Table 1 (continued)

Spot	Th/U	Isotopic ratios						Isotopic ages			
		$^{206}Pb/^{238}U$	1σ	$^{207}Pb/^{235}U$	1σ	$^{207}Pb/^{206}Pb$	1σ	$^{206}Pb/^{238}U$	1σ	$^{207}Pb/^{235}U$	1σ
GS0820.2	1.48	0.11821	0.01018	0.02204	0.00020	0.03998	0.00336	140.5	1.3	113.5	8.7
GS0820.3	1.83	0.11408	0.01234	0.02199	0.00020	0.03771	0.00402	140.2	1.3	109.7	10.9
GS0820.4	1.87	0.24528	0.03734	0.02223	0.00032	0.07938	0.01172	141.8	1.7	222.7	15.3
GS0820.5	1.14	0.20546	0.01814	0.02226	0.00023	0.06673	0.00604	141.9	1.4	189.7	8.9
GS0820.6	1.75	0.13728	0.00672	0.02228	0.00020	0.04479	0.00216	142.0	1.3	130.6	5.0
GS0820.7	1.25	0.09992	0.01433	0.02189	0.00022	0.03403	0.00477	139.6	1.4	96.7	14.4
GS0820.8	2.30	0.14761	0.00907	0.02146	0.00016	0.04980	0.00305	136.9	1.2	139.8	6.3
GS0820.9	1.58	0.15236	0.03070	0.02145	0.00027	0.05513	0.01112	136.8	1.6	144.0	20.2
GS0820.10	1.84	0.20331	0.01630	0.02179	0.00020	0.06723	0.00533	138.9	1.3	187.9	8.1
GS0820.11	1.55	0.15622	0.00781	0.02203	0.00017	0.05140	0.00250	140.5	1.2	147.4	5.1
GS0820.12	1.26	0.19058	0.01965	0.02439	0.00022	0.05708	0.00589	155.4	1.3	177.1	10.4
GS0820.13	1.54	0.14899	0.00989	0.02197	0.00019	0.04963	0.00332	140.1	1.3	141.0	6.8
GS0820.14	2.53	0.19791	0.03035	0.01971	0.00023	0.07027	0.01073	125.8	1.5	183.4	15.4
GS0820.15	1.66	0.14437	0.01153	0.02095	0.00016	0.05041	0.00406	133.6	1.2	136.9	8.1
GS0820.16	1.69	0.14294	0.00738	0.02100	0.00016	0.04925	0.00253	134.0	1.2	135.7	5.3
GS0820.17	2.32	0.19035	0.01617	0.02235	0.00022	0.06231	0.00524	142.5	1.3	176.9	8.6
GS0820.18	2.66	0.16513	0.00754	0.02196	0.00017	0.05478	0.00246	140.0	1.2	155.2	4.7
GS0820.19	3.50	0.15492	0.01647	0.02070	0.00017	0.05371	0.00576	132.1	1.2	146.2	10.7
GS0820.20	2.43	0.15334	0.01569	0.02179	0.00020	0.05062	0.00525	138.9	1.3	144.9	10.3
GS0820.21	1.61	0.27461	0.03453	0.02225	0.00032	0.09604	0.01222	141.8	1.7	246.4	12.6
GS0820.22	1.64	0.21376	0.03403	0.02192	0.00028	0.06807	0.01174	139.8	1.6	196.7	16.0

the field of granite in the TAS diagram (Fig. 5a). The 22 samples exhibit high SiO_2 (71.5–77.6 wt%), Na_2O (3.1–4.5 wt%), K_2O (4.5–5.4 wt%), Al_2O_3 (12.0–14.3 wt%) contents, and low and variable MgO contents with $Mg^{\#}$ = 6–55. The samples are weekly peraluminous with most A/CNK [Al_2O_3/($CaO+Na_2O+K_2O$)] values lower than 1.1 (0.98–1.11, Fig. 5c) and belong to high-K calc-alkaline series (Fig. 5d). Al_2O_3, FeOT, MgO, CaO, TiO_2, and P_2O_5 show negative correlations with SiO_2 (Fig. 6). The negative correlations of Na_2O+K_2O with SiO_2 are insignificant. They show LREE-enriched chondrite-normalized REE patterns with strongly Eu anomalies (Eu* = 0.16–0.73; Fig. 7a). On the primitive mantle-normalized spidergram (Fig. 7b), the syenogranite samples exhibit significantly negative anomalies of Nb, Ta, Sr, P, and Ti.

Rhyolite

The rhyolite samples are highly siliceous (Table 2), with SiO_2 contents ranging from 71.8 wt.% to 80.0 wt.% and were plotted mainly in the field of rhyolite in Fig. 5b. They have relatively high alkali contents with K_2O = 4.4–5.6 wt.% and Na_2O = 2.7–4.3 wt.%, and the total K_2O+Na_2O contents varying from 7.1 to 9.9 wt.%. The samples are classified as high-K calc-alkaline series according to the K_2O versus SiO_2 classification scheme (Fig. 5d). They are weakly peraluminous with A/CNK ratios between 0.99 and 1.10. Al_2O_3, FeOT, MgO, CaO, Na_2O+K_2O, TiO_2, and P_2O_5 show negative correlations with SiO_2 (Fig. 6). The rhyolite samples show LREE-enriched chondrite-normalized REE patterns with significant Eu anomalies (Eu* = 0.16–0.52; Fig. 7a). On the multi-elemental primitive mantle-normalized spider diagram (Fig. 7b), these samples are characterized by strong depletions in Nb, Ta, Sr, P, and Ti.

Discussion

Genetic type: I-type, S-type, or A-type?

Based on chemical and mineralogical criteria, granitoid rocks have traditionally been classified as I-, S-, and A-types (Chappell and White 1974, 1992; Hineab et al. 1978; Whalen et al. 1987). A-type granitoid typically contains high-temperature anhydrous minerals, such as pyroxene, fayalite, and interstitial biotite (Collins et al. 1982; Eby 1992; Whalen et al. 1987). A-type granitoids are also characterized by high FeOT/MgO ratios and the enrichment of the HFSE and REE concentrations with Zr higher than 250 ppm and Zr + Nb + Ce + Y higher than 350 ppm (Eby 1990, 1992; Frost and Frost 2011). Both our rhyolites and syenogranites samples show low FeOT/MgO ratios, Zr

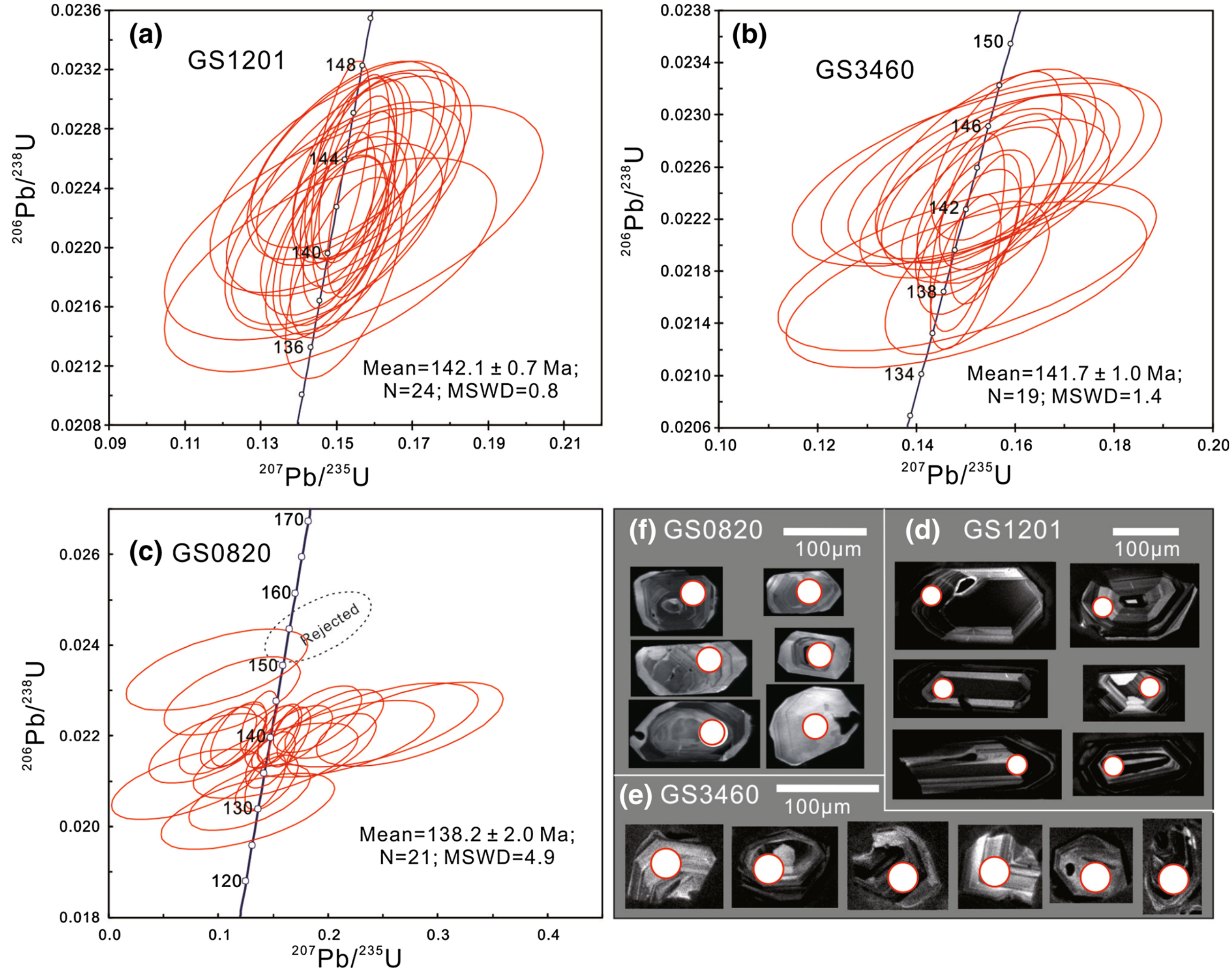

Fig. 4 **a–c** LA-ICP-MS zircon U-Pb concordia diagrams for the Tuoliela syenogranite (GS1201), Wuertu syenogranite (GS3460), and Hanwula rhyolite (GS0820). **d–f** Cathodoluminescence (CL) images of representative zircon grains. Red circles on CL images mark analytical site on each grain

and Zr + Nb + Ce + Y contents except one rhyolite sample (GS0820; Fig. 8). Besides, no high-temperature anhydrous minerals (pyroxene, fayalite, or interstitial biotite) have been observed in the rhyolite and syenogranite samples (Supplemental file 1). These mineral and chemical characteristics indicate that our rhyolites and syenogranites are not A-type granites.

S-type granites were first recognized as strongly peraluminous magmas derived (dominantly) from metasedimentary rocks. Thus, S-type granites typically contain abundant inherited zircon (Collins and Richards 2008) and Al-rich minerals, such as muscovite, garnet, and cordierite, and are always strongly peraluminous with high A/CNK (> 1.1; Chappell 1999; Chappell and White 1992; Clemens 2003). In contrast, I-type granites were identified to be derived from the meta-igneous rocks, and contain hornblende, especially at the more mafic end of the compositional spectrum (Chappell et al. 1998; Chappell and White 1992; Roberts and Clemens 1993). I-type granites are always metaluminous to weakly peraluminous with the A/CNK ratios lower than 1.1 (Chappell 1999; Chappell and White 1992). Besides, the negative correlation between P_2O_5 and SiO_2 is a crucial criterion for distinguishing the I-type granites from S-type granites (Chappell and White 1992). Our syenogranite samples contain some hornblendes. Both the rhyolites and syenogranites samples show low A/CNK ratios (< 1.1) and notable negative correlations between P_2O_5 and SiO_2 (Fig. 6f). Besides, the rhyolites of the Baiyingaolao formation show high and positive zircon $\varepsilon_{Hf}(t)$ values (2.6–12.1; supplemental file 2; Dong et al. 2014). Therefore, the rhyolites and syenogranites are more likely to be I-type granitoids, rather than the S-type.

Table 2 Major (wt%) and trace elemental (ppm) analyzed results for the Early Cretaceous rhyolites and syenogranites in Erguna and Xing'an massifs

Sample	GS1201	GS2529	GS3153	GS3132	GS6091	GS2031	GS6113	GS007	GS007	GS008	GS2539	GS4121	GS3125	GS2037	GS4128
Tuoliela syenogranite															
SiO_2	73.34	74.92	72.81	73.21	74.44	72.4	71.54	73.65	73.33	72.61	75.12	75.41	75.79	75.41	76.16
TiO_2	0.26	0.22	0.32	0.26	0.22	0.32	0.33	0.27	0.28	0.31	0.18	0.18	0.17	0.17	0.18
Al_2O_3	13.73	12.52	14.32	14.04	13.6	14.17	13.89	13.47	13.96	14.27	12.55	12.72	12.62	13.17	12.58
Fe_2O_3	1.08	0.88	0.98	1.15	1.00	1.07	1.53	1.55	1.44	1.55	0.94	0.91	0.85	0.82	1.09
FeO	0.56	0.53	0.81	0.51	0.67	1.01	1.02	0.35	0.45	0.49	0.36	0.35	0.55	0.47	0.14
MnO	0.08	0.06	0.09	0.09	0.08	0.09	0.07	0.07	0.08	0.09	0.04	0.04	0.02	0.02	0.02
MgO	0.36	0.80	0.40	0.34	0.24	0.45	0.48	0.27	0.29	0.36	0.71	0.30	0.10	0.11	0.12
CaO	0.78	0.59	0.82	0.77	0.59	0.86	0.96	0.74	0.74	0.84	0.50	0.42	0.35	0.37	0.40
Na_2O	3.88	3.99	4.15	4.1	3.88	4.37	4.52	3.82	3.88	3.99	3.55	3.63	3.79	3.80	3.70
K_2O	4.68	4.77	4.70	4.87	4.76	4.66	4.63	4.70	4.46	4.65	5.01	5.05	4.89	4.94	4.72
P_2O_5	0.09	0.05	0.12	0.07	0.07	0.08	0.09	0.07	0.06	0.07	0.03	0.09	0.01	0.02	0.01
LOI	0.64	0.47	0.31	0.44	0.32	0.60	0.87	0.56	0.44	0.44	0.71	0.56	0.66	0.65	0.58
Total	99.49	99.8	99.83	99.85	99.87	100.08	99.93	99.52	99.42	99.66	99.7	99.66	99.8	99.95	99.71
V	59.9	20.0	17.0	15.0	19.0	17.3	16.9	15.0	14.0	17.0	13.0	16.0	7.11	5.61	6.56
Cr	56.9	69.0	54.4	34.4	46.7	17.2	18.0	14.0	8.00	11.0	60.2	31.4	21.7	13.0	21.5
Co	5.08	2.60	2.73	1.53	1.90	2.17	3.27	1.67	2.14	2.29	4.10	3.50	1.33	1.20	1.03
Ni	6.50	26.9	28.8	14.6	17.1	3.42	2.13	8.65	10.1	9.08	31.2	18.5	3.14	2.91	2.36
Rb	172	151	146	161	130	200	190	188	186	179	182	179	190	190	190
Sr	144	128	137	141	133	130	110	117	156	169	48.0	46.0	65.0	60.0	59.0
Y	22.1	19.8	18.4	13.2	15.5	18.3	19.2	18.4	17.5	20.2	10.6	10.2	11.8	12.6	11.7
Zr	142	198	190	184	228	200	190	170	163	184	133	131	150	130	160
Nb	12.9	16.9	14.4	13.6	16.1	15.7	19.8	15.8	14.6	18.1	16.4	15.7	15.7	16.7	19.1
Ba	375	586	502	609	529	540	570				300	318	240	240	240
La	28.1	36.4	39.2	35.1	28.1	43.2	26.6	34.5	36.0	39.2	29.4	28.8	26.0	23.5	22.9
Ce	58.9	69.8	62.3	58.5	45.8	75.3	52.9	63.7	65.1	71.3	52.1	58.1	30.5	29.3	27.5
Pr	5.78	8.05	7.16	6.32	5.16	7.57	6.13	6.99	7.06	7.82	5.20	5.04	4.28	4.09	3.82
Nd	19.6	27.3	23.3	20.2	17.4	24.9	22.6	24.7	25.3	27.4	15.8	15.4	13.1	13.6	12.0
Sm	3.52	4.54	3.69	3.12	2.95	4.60	4.27	4.10	4.16	4.54	2.37	2.26	2.31	2.26	2.15
Eu	0.700	0.930	0.750	0.730	0.700	0.820	0.800	0.820	0.920	0.880	0.500	0.510	0.410	0.410	0.400
Gd	3.21	4.56	3.90	3.01	3.01	4.24	3.83	3.64	3.71	4.16	2.36	2.37	2.23	2.33	2.10
Tb	0.540	0.640	0.540	0.430	0.450	0.600	0.620	0.570	0.560	0.620	0.320	0.320	0.340	0.340	0.320
Dy	3.38	3.20	2.67	2.08	2.37	3.13	3.41	3.10	3.01	3.40	1.56	1.53	1.99	2.13	1.99
Ho	0.650	0.610	0.520	0.390	0.470	0.580	0.640	0.630	0.610	0.700	0.310	0.310	0.390	0.440	0.380
Er	2.27	2.27	1.97	1.51	1.74	1.92	1.94	1.84	1.78	2.04	1.32	1.29	1.33	1.42	1.31
Tm	0.350	0.390	0.340	0.260	0.300	0.350	0.360	0.320	0.320	0.370	0.250	0.250	0.320	0.280	0.290

Table 2 (continued)

Sample	GS1201	GS2529	GS3153	GS3132	GS6091	GS2031	GS6113	GS007	GS007	GS008	GS2539	GS4121	GS3125	GS2037	GS4128
Tuoliela syenogranite															
Yb	2.20	2.49	2.30	1.75	1.92	2.40	2.52	2.21	2.14	2.47	1.91	1.84	2.07	2.03	1.76
Lu	0.360	0.360	0.330	0.260	0.290	0.400	0.370	0.370	0.370	0.420	0.300	0.280	0.330	0.320	0.330
Ta															
Th	12.2					21.9	23.7	26.4	24.0	28.0			25.7	22.0	23.7
U	1.90	2.64	2.80	2.55	2.80	2.64	3.98	4.53	2.26	2.69	3.52	3.66	8.24	9.06	9.78
FeOT	1.53	1.32	1.69	1.54	1.57	1.97	2.40	1.74	1.75	1.88	1.21	1.17	1.31	1.21	1.12
Mg#	33	56	33	32	24	32	30	25	26	29	55	35	14	16	18
A/CNK	1.07	0.98	1.07	1.05	1.08	1.03	0.98	1.06	1.11	1.09	1.03	1.04	1.04	1.07	1.06
TZr (°C)	824	852	851	848	871	853	844	841	838	850	819	817	828	818	835

Sample	GS-1	GS-2	GS5750	GS5751	GS57511	GS57512	GS3460	GS8204	GS0820	GS3273	GS4017
	Wuertu syenogranite							Hanwula rhyolite			
SiO_2	77.18	76.13	77.6	73.9	72.66	73.73	75.42	76.74	71.75	76.3	80.03
TiO_2	0.06	0.07	0.07	0.30	0.36	0.35	0.22	0.19	0.58	0.19	0.10
Al_2O_3	12.58	12.85	12.01	12.44	13.85	13.06	12.76	12.53	13.69	12.41	10.49
Fe_2O_3	0.43	0.2	0.71	1.21	1.23	1.06	1.42	0.27	1.81	0.72	0.93
FeO	0.54	0.8	0.42	0.83	0.84	0.95	0.27	0.37	0.52	0.098	0.21
MnO	0.05	0.06	0.06	0.07	0.08	0.07	0.09	0.01	0.05	0.03	0.03
MgO	0.05	0.06	0.03	0.32	0.42	0.43	0.28	0.08	0.23	0.07	0.08
CaO	0.28	0.34	0.34	0.45	0.72	0.72	0.52	0.44	0.38	0.18	0.21
Na_2O	3.66	4.35	3.12	3.62	3.70	3.71	3.56	3.68	4.28	3.8	2.65
K_2O	4.92	4.9	4.95	5.44	4.98	4.96	4.86	5.02	5.61	5.28	4.43
P_2O_5	0.01	0.01	0.02	0.07	0.12	0.05	0.05	0.03	0.06	0.02	0.02
LOI	0.2	0.14	0.33	0.54	0.46	0.60	0.46	0.62	0.98	0.89	0.82
Total	99.96	99.91	99.65	99.19	99.42	99.69	99.9	99.973	99.936	99.984	99.993
V	2.3	3.23	4	25.5	21	23	41.6	8.71	15.9	2.91	7.77
Cr	2.76	2.74	35.7	38.3	32.4	20.5	14	2.75	2.57	2.3	14.1
Co	0.38	0.38	0.81	2.59	2.14	2.26	2.11	1.05	1.46	0.93	0.51
Ni	1.91	1.57	16.3	17.7	15.1	11.3	3.41	0.45	0.85	0.53	7.17
Rb	143	156	139	201	194	206	239	222	142	200	91.2
Sr	10.4	12.3	18.4	139	138	146	49.1	56	66.2	21.2	51.3
Y	7.8	8.61	11	12.8	8.27	18.7	10.2	11.7	24.2	15.5	18.6
Zr	97.9	111	121	262	185	210	138	137	559	213	140
Nb	22.6	24.2	20.4	23.7	19.5	20.7	25.2	17.6	26.9	25.3	7.36
Ba	15	17.5	47	365	366	383	494	74	307	21.5	789

Table 2 (continued)

Sample	GS-1	GS-2	GS5750	GS5751	GS57511	GS57512	GS3460	GS8204	GS0820	GS3273	GS4017
	Wuertu syenogranite							Hanwula rhyolite			
La	3.71	4.41	9.38	48.5	37.6	55.6	35.2	42.8	90.6	23.3	25.2
Ce	9.51	10.5	23.6	91.2	66.8	97.7	51.8	80.5	168	54.6	52.1
Pr	1.1	1.33	2.51	9.77	5.79	10.9	5.47	8.34	21	5.48	6.28
Nd	4.12	5.25	9.43	31.5	17.3	35.1	16.9	28	75.6	18.5	23.7
Sm	0.97	1.24	2.06	4.71	2.54	5.37	2.56	4.49	11.7	3.83	4.32
Eu	0.054	0.071	0.16	0.88	0.54	0.99	0.54	0.56	1.8	0.19	0.61
Gd	1.12	1.53	1.74	4.81	2.79	6.19	2.35	3.93	9.75	3.31	4.15
Tb	0.22	0.25	0.35	0.59	0.33	0.69	0.33	0.52	1.23	0.54	0.62
Dy	1.54	1.62	1.93	2.54	1.45	3.02	1.77	2.46	5.56	3.1	3.76
Ho	0.34	0.34	0.38	0.45	0.27	0.56	0.31	0.45	0.96	0.59	0.8
Er	0.97	0.95	1.35	1.61	1.04	2.08	1.13	1.15	2.44	1.57	2.41
Tm	0.16	0.14	0.24	0.26	0.18	0.33	0.19	0.18	0.37	0.24	0.38
Yb	1.03	0.93	1.62	1.79	1.31	2.25	1.3	1.21	2.39	1.65	2.62
Lu	0.16	0.15	0.23	0.25	0.19	0.31	0.26	0.18	0.36	0.24	0.41
Ta								1.4	1.57	1.74	0.55
Th	10.3	9.31					22	23.8	16.4	17.4	9.3
U	1.24	1.12	2.05	4.72	3.75	3.85	2.63	2.55	2.77	5.14	1.92
FeOT	0.93	0.98	1.06	1.92	1.95	1.9	1.55	0.61	2.15	0.75	1.05
Mg#	10	11	6	26	31	32	28	21	18	16	14
A/CNK	1.06	0.98	1.08	0.98	1.08	1.02	1.06	1.02	0.99	1.01	1.1
TZr (°C)	794	798	813	882	847	859	822	821	965	860	848

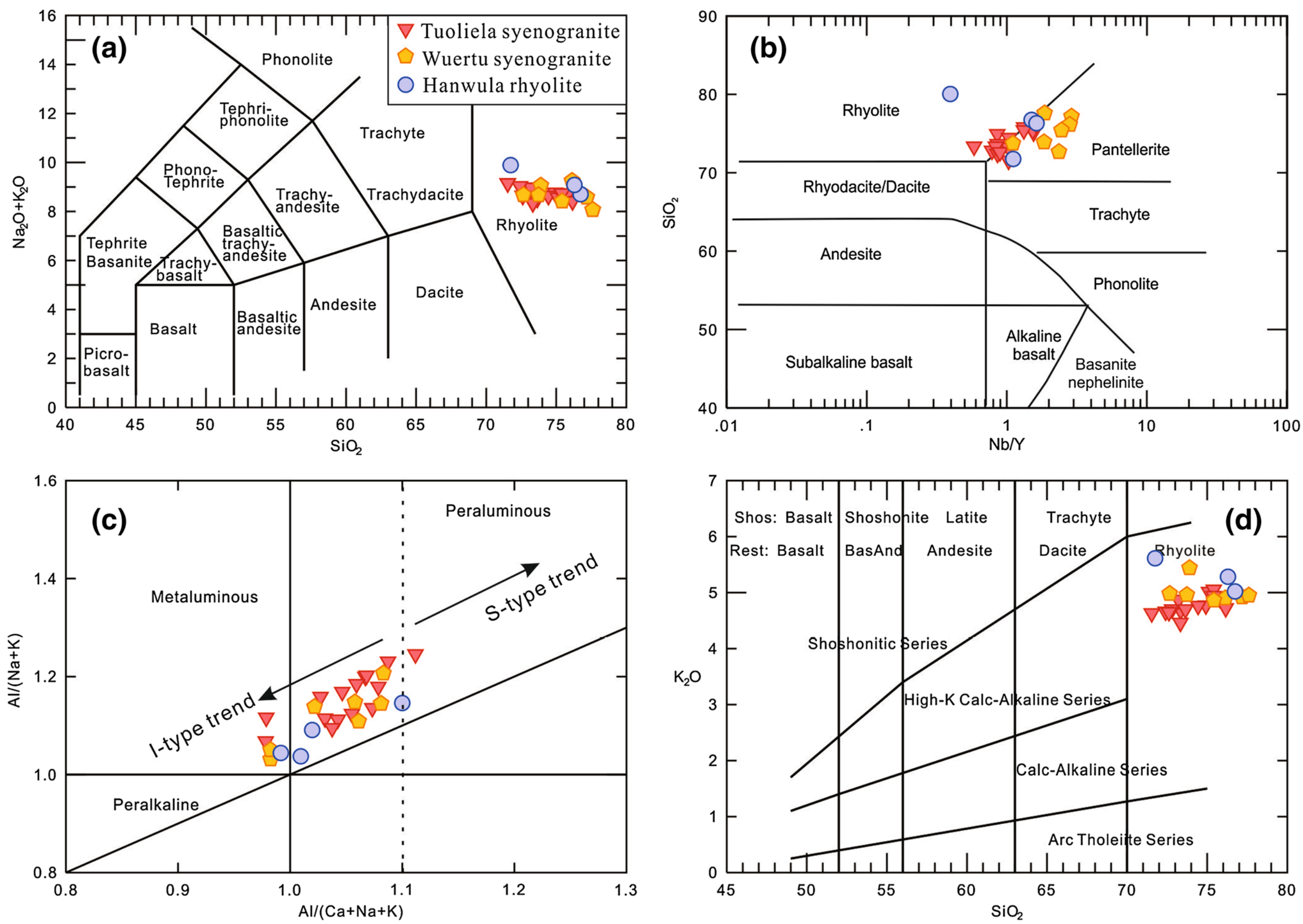

Fig. 5 **a** SiO_2 – (K_2O+Na_2O) plot (Le Bas et al. 1986). **b** Nb/Y-SiO_2 plot (Winchester and Floyd 1977). **c** A/CNK [molar Al_2O_3/($CaO+Na_2O+K_2O$)] versus SiO_2 diagram, and (d) K_2O versus SiO_2 diagram (Le Maitre et al. 1989)

Petrogenesis of the early cretaceous rhyolites and syenogranites

Our rhyolites and syenogranite samples fall in the fields of high-K calc-alkaline series in Fig. 4d. According to Barbarin (1999), they could be classified as high-K calc-alkaline I-type granitoids. Such granitoids were derived from (1) fractional crystallization of mantle-derived basaltic magma coupled with crustal contamination (Barth et al. 1995), (2) mixing of mantle-derived mafic magma and crust-derived felsic magma (Cong et al. 2011; Yang et al. 2016), or (3) partial melting of sub-alkaline meta-basalts, followed by fractionation (Rapp and Watson 1995). The products from either case (1) or (2) usually show low SiO_2, but high Al_2O_3 (> 14.5 wt%) and Na_2O contents ($Na_2O/K_2O > 1$), and contain abundant inherited zircons. Besides, the products from case (1) are generally associated with large volumes of mafic–intermedia rocks, and mafic microgranular enclaves (MME) may occur in case (2) (Barbarin 2005). However, our rhyolites and syenogranites samples show high SiO_2 (up to 80.0 wt%), low Al_2O_3 (10.5–14.3 wt.%) and Na_2O/K_2O ratios (0.60–0.98). Only limited volumes of mafic–intermedia rocks crop out in this area and MMEs are absent in the syenogranite plutons (Supplemental file 1). Experimental studies have demonstrated that partial melting of basaltic rocks can produce intermediate-to-silicic melts leaving a granulite residue at 8–12 kbar or an eclogite residue at 12–32 kbar (Rapp and Watson 1995). Thus, it is likely that the rhyolites and syenogranites are originated from partial melting of sub-alkaline meta-basalts.

The I-type granites may be classified into two distinct types, high- and low-temperature, based on the absence or presence, respectively, of initially inherited zircons (Chappell et al. 1998). Our three age dating samples only contain two inherited zircons. The inherited zircons show young $^{206}Pb/^{238}U$ ages of 172 and 155 Ma, which may be from the surrounding Middle Jurassic granites and the underlain Manitu formation, respectively. They are from wall rocks, rather than initially inherited. We carried out whole-rock zirconium saturation temperature (T_{Zr}) calculation and got the T_{Zr} in a range of 794–881 °C and 803–964 °C for the syenogranites and rhyolites, respectively. Thus, the rhyolites and

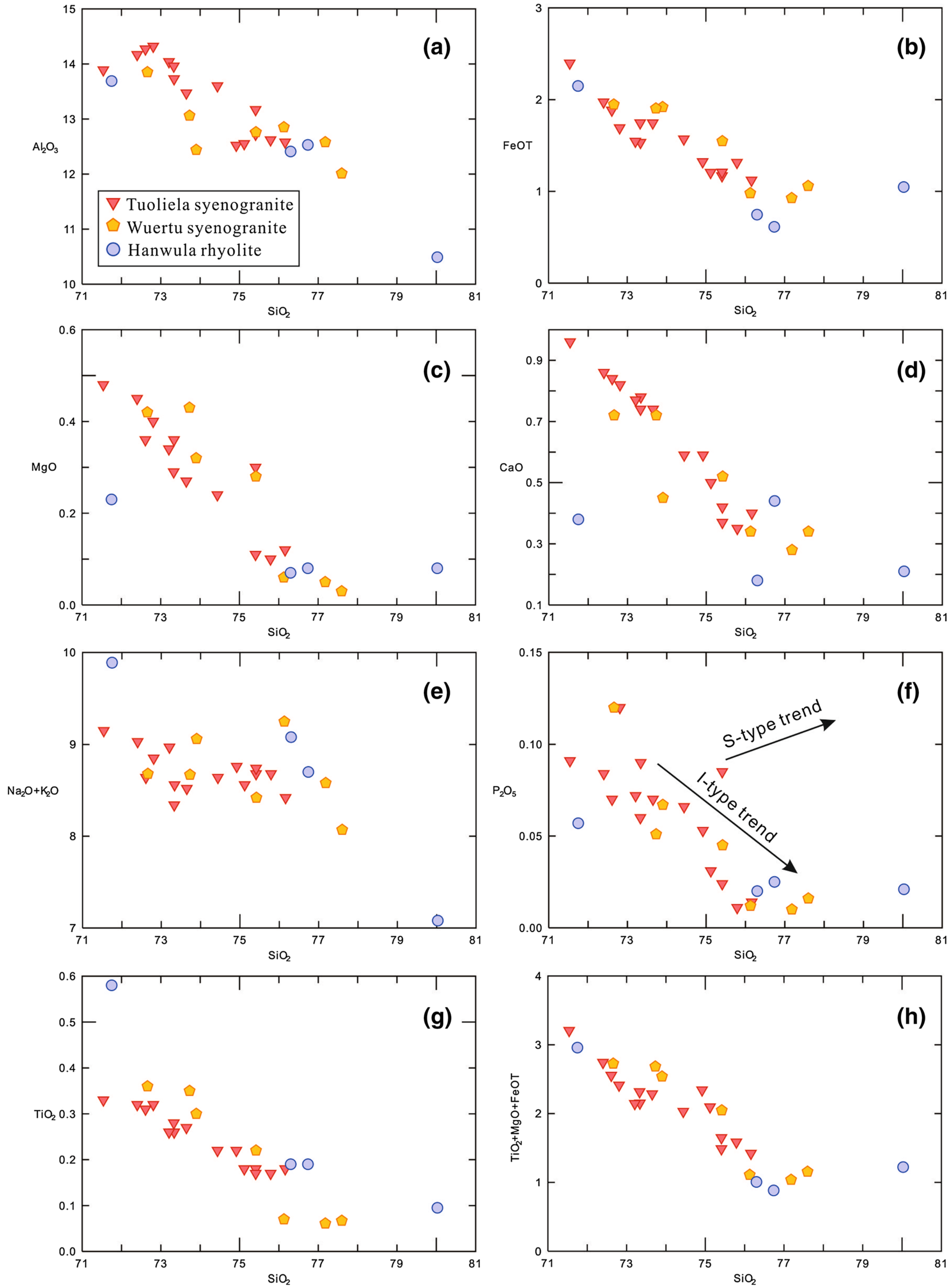

Fig. 6 Harker diagrams for the Early Cretaceous rhyolites and syenogranites in Erguna and Xing'an massifs. Symbols are the same as in Fig. 5

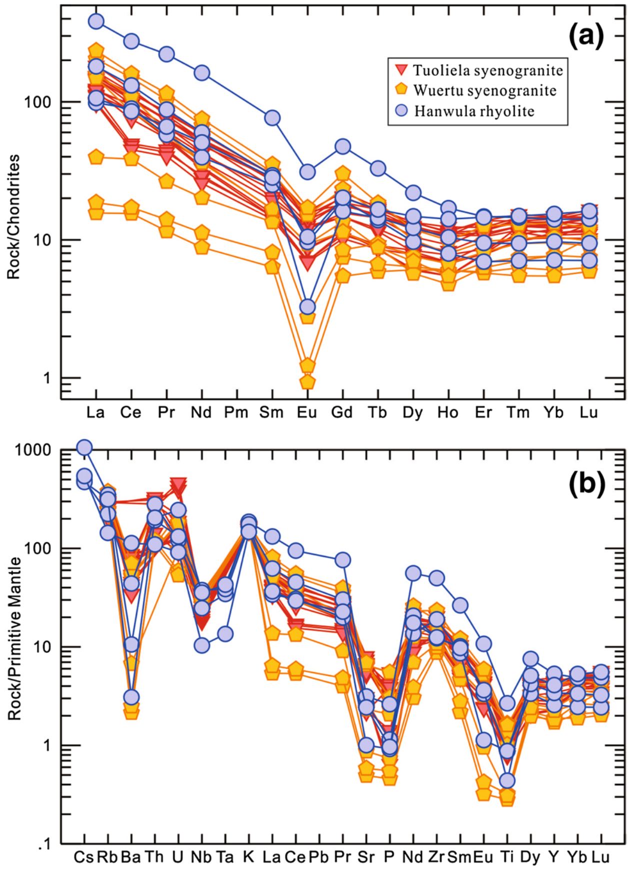

Fig. 7 Primitive mantle-normalized incompatible elemental spidergrams and chondrite-normalized REE patterns for the Early Cretaceous rhyolites and syenogranites in Erguna and Xing'an massifs. Normalized values for primitive mantle and chondrite are from reference (Sun and McDonough 1989)

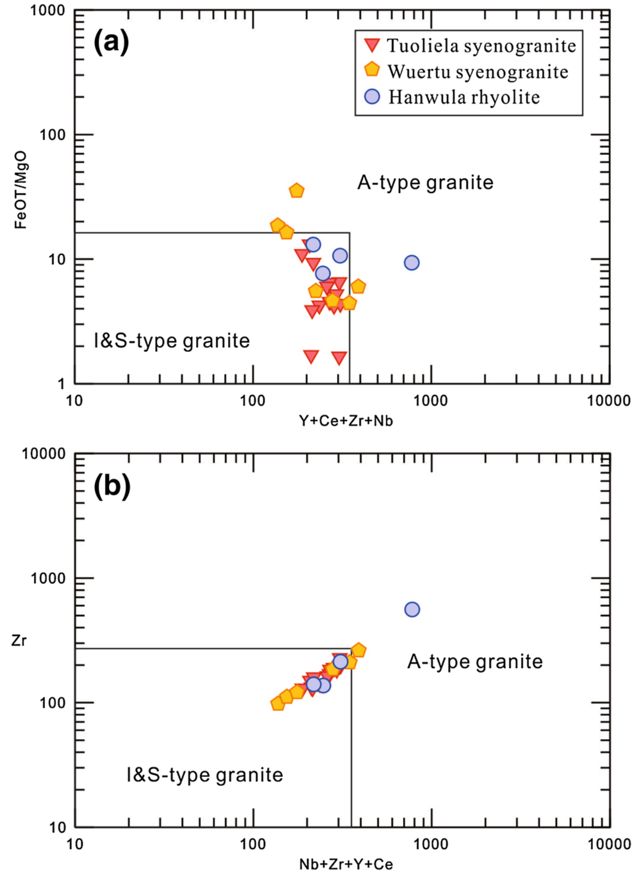

Fig. 8 **a** FeOT/MgO versus (Zr + Nb + Ce + Y) (ppm) plot (Whalen et al. 1987) and **b** Zr (ppm) versus (Zr + Nb + Ce + Y) (ppm) plot (Whalen et al. 1987). Symbols are the same as in Fig. 5

syenogranites should be high-temperature I-type granitoids. The high-temperature I-type granites formed from a magma that was completely or largely molten (Chappell et al. 1998). Experiments reveal that water-unsaturated dehydration melting of the meta-basalts can generate mildly peraluminous melt with high-K content (Chappell et al. 2012; Rapp and Watson 1995), and water-saturated melting of the meta-basalts yields strong peraluminous melts enriched in Ca and depleted in Fe, Mg, and K (Beard and Lofgren 1991). The rhyolites and syenogranites are weakly peraluminous and K-enriched, and they should be generated by water-unsaturated dehydration melting of the meta-basalts. Experimental data have demonstrated that biotite and muscovite will breakdown when the temperature is higher than 800–850 °C (Thompson and Connolly 1995), but dehydration melting of amphibolites requires much higher temperatures (> 1000 °C, Rapp and Watson 1995). Rb/Sr and Ba show negative connections, which are also in accordance with the dehydration melting of biotite/muscovite (Fig. 9). Residual mineral assembles after melt extraction may also play a crucial role

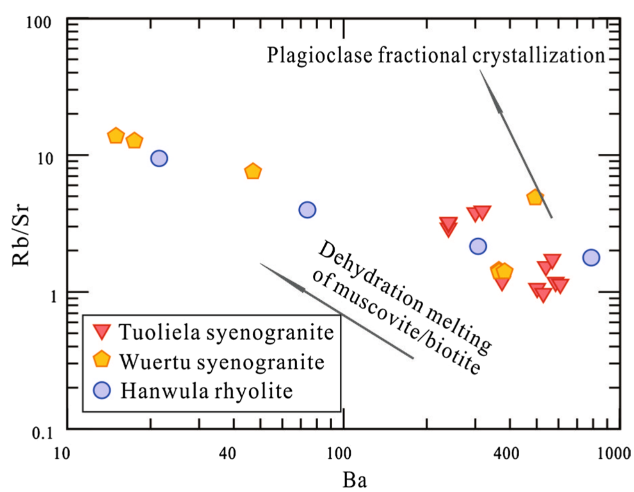

Fig. 9 Rb/Sr versus Ba for the Early Cretaceous rhyolites and syenogranites in Erguna and Xing'an massifs. The trends for dehydration muscovite and biotite melting and plagioclase fractional crystallization are from Zhang et al. (2004)

in forming magmas with peculiar geochemical characteristics (Beard and Lofgren 1991). Low HREE abundances and fractionated REEs indicate the possible presence of garnet in the residuum. The flat HREE patterns may suggest amphibole as another residual mineral. Figure 9 and insignificant negative correlations of Na_2O+K_2O with SiO_2 in Fig. 6 show that plagioclase fractional crystallization was insignificant, but our samples show notable negative Eu and Sr negative anomalies (Fig. 7), implying that plagioclase might also play as residual mineral in the magma chamber (Martin 1999). Thus, the rhyolites and syenogranites were generated by dehydration melting of biotite/muscovite from sub-alkaline meta-basalts, leaving garnet, amphibole, and plagioclase as the major residual minerals.

Tectonic setting

High-K calc-alkaline I-type granites may be generated in two tectonic scenarios: (1) continental arc settings like that of the Andes and (2) post-collisional settings like that of the Caledonides (Roberts and Clemens 1993). In the case of Early Cretaceous rhyolites and syenogranites in Erguna and Xing'an massifs, three tectonic models may account for their generation, including (1) post-collisional extension related to the Paleo-Asian Ocean closure, (2) post-collisional extension related to the closure of the Mongol–Okhotsk Ocean, and (3) the Mongol–Okhotsk oceanic and/or Paleo-Pacific subduction setting (Cogne et al. 2005; Dong et al. 2014; Ji et al. 2016; Tang et al. 2015; Wang et al. 2015b, c; Yang et al. 2015). The final closure of the Paleo-Asian Ocean may occurred at Middle Permian, Late Permian, or Middle Triassic, and that the associated collisional orogeny terminated at Late Triassic (Chen et al. 2015; Wang et al. 2015c; Yang et al. 2017; Zhou et al. 2017). The transition from the Paleo-Asian oceanic regime to the circum-Pacific tectonic regime in NE China may took place during the Late Triassic-to-Early Jurassic (Yang et al. 2017). Post-collisional extension often happened 10–20 Ma later of the final closure of the ancient ocean (Wang et al. 2007). Therefore, it seems impossible for the Early Cretaceous rhyolites and syenogranites to be formed in a post-collisional setting related to the Paleo-Asian Ocean closure.

Palaeomagnetic studies revealed that the Mongol–Okhotsk ocean did not close until the end of Early Cretaceous (Kravchinsky et al. 2002) or later (Halim et al. 1998). These observations indicate that petrogenesis of the Early Cretaceous rhyolites and syenogranites cannot be controlled by post-collisional extension related to the closure of the Mongol–Okhotsk Ocean. Eastern central Asia was an active continental margin during the early Mesozoic, and closely associated with subduction of the Mongol–Okhotsk plate to the north (Halim et al. 1998; Kravchinsky et al. 2002) and the Paleo-Pacific plate to the east (Zhou and Wilde 2013). On the discrimination diagrams of Rb versus Y + Nb and Nb versus Y (Pearce et al. 1984), all the samples fall in the field of arc volcanic granite (Fig. 10). Thus, the Early Cretaceous rhyolites and syenogranites may be generated in the Mongol–Okhotsk oceanic or Paleo-Pacific subduction settings (Case 3). However, the Early Cretaceous igneous rocks are characterized by NE-trending zonation (parallel to the Mongol–Okhotsk suture) and is well distinguished from Paleo-Pacific subduction induced magmatism in the Songliao basin (Fig. 1b; Zhang 2014). Besides, the Early Cretaceous igneous rocks in the western Erguna and Xing'an

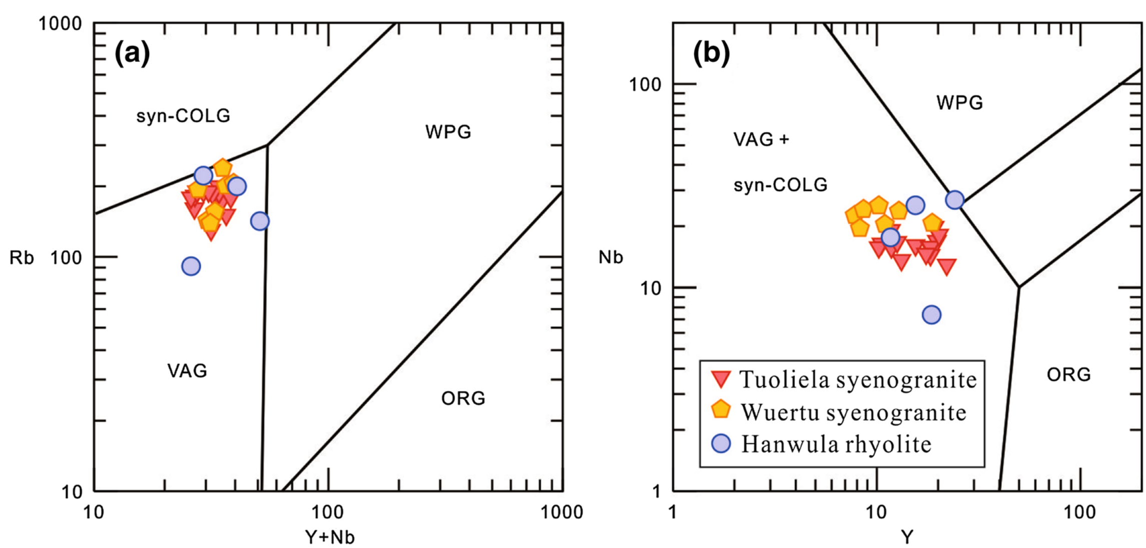

Fig. 10 Tectonic discrimination diagrams for the Early Cretaceous rhyolites and syenogranites in Erguna and Xing'an massifs involving **a** Rb-(Y + Nb) and **b** Nb–Y diagrams (Pearce et al. 1984). Symbols are the same as in Fig. 5

massifs are also relatively far from the Pacific subduction zone but near the Mongol–Okhotsk suture (Fig. 1b). Thus, a more plausible setting for the Early Cretaceous rhyolites and syenogranites is the Mongol–Okhotsk oceanic subduction. Zhang (2014) proposed a ridge subduction and slab window model for the petrogenesis of the large-scale igneous rocks in the Erguna and Xing'an massifs (Fig. 11). The thermal budget provided by radioactive decay or crustal thickening would not be sufficient to trigger the partial melting of the sub-alkaline meta-basalts without additional heat input from the mantle processes. The underplating of asthenospheric mantle associated with the ridge subduction and slab window during the Mongol–Okhotsk oceanic subduction may provide the likely heat source (Fig. 11).

Early cretaceous lower crustal reworking

One question remains as where the source rocks (i.e., the sub-alkaline meta-basalts) of the Early Cretaceous rhyolites and syenogranites were located, in upper, middle, or lower continental crust? The upper continental crust shows equal chemical compositions with the granites, the lower continental crust shows equal chemical compositions with the basalts, and the middle crust shows transitional chemical compositions between them (Rudnick 1995; Rudnick and Fountain 1995). Source rocks of the Early Cretaceous rhyolites and syenogranites are geochemically identical to the lower continental crust. Besides, our samples show high T_{Zr} (794–964 °C), suggesting that their generation should not be shallower than the lower continental crust. Thus, the source rocks (i.e., the sub-alkaline meta-basalts) may be parts of the lower continental crust in NE China, and their dehydration melting may represent the partial melting of lower continental crust. The recycled melt was transferred to the upper crust, produced the rhyolites and syenogranites, and caused the chemical differentiation of the continental crust. This process was identified as the lower crustal reworking.

Although much less attention has been paid to the Phanerozoic crustal reworking in NE China, the following observations indicate that Early Cretaceous lower crustal reworking in NE China may be rather pronounced. (1) The volcanic rocks of the Manketouebo and Baiyingaolao Formations are widespread in Erguna and Xing'an massifs, which were proposed to be derived from the partial melting of Neoproterozoic-to-Phanerozoic juvenile crustal material (Dong et al. 2014; Ji et al. 2016). (2) Large volumes of Early Cretaceous acidic rocks crop out in Songliao basin as products of juvenile crustal remelting (Guo et al. 2009; Huang et al. 2010; Pei et al. 2010; Wang et al. 2010, 2002; Zhang et al. 2011). (3) Many I-type and A-type granitic plutons in Khanka, Jiamusi, Songnen–Zhangguangcai Range, Xing'an, and Erguna massifs were previously believed to represent crustal growth (Guo et al. 2009; Liu et al. 2015; Wang et al. 2015b; Yang et al. 2014). However, these granites are also derived from melting of juvenile mafic lower crust (Guo et al. 2009); surely, they are products of lower crustal reworking.

Incorporating all these materials, we argue that Early Cretaceous crustal reworking is widely distributed in NE China.

Conclusions

(a) Early Cretaceous zircon U–Pb ages of 142–138 Ma were obtained for the syenogranites and rhyolites in the western Great Xing'an range (NE China).
(b) The syenogranites and rhyolites show low Zr and Zr + Nb + Ce + Y contents, and low A/CNK, $Mg^{\#}$, and FeOT/MgO values. They are K_2O-enriched and yield negative correlations between P_2O_5 and SiO_2. Both were classified as high-K calc-alkaline I-type granitoids.
(c) The syenogranites and rhyolites were generated by dehydration melting of biotite/muscovite from sub-

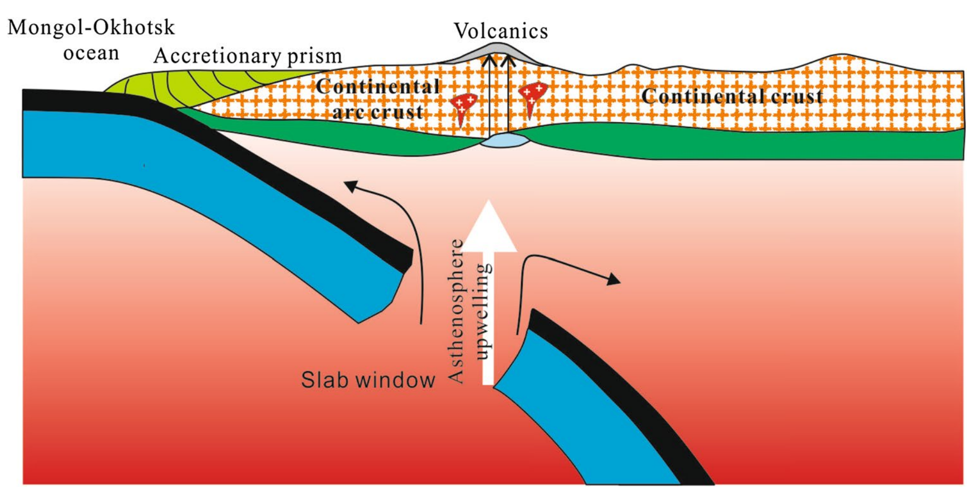

Fig. 11 Schematic diagram for the Early Cretaceous tectonic enviroments of the western Erguna and Xing'an massifs (China). The ridge subduction and slab window of Mongol–Okhotsk ocean induced the asthenosphere upwelling which provided the likely heat source for the partial melting of the meta-basaltic source rocks

alkaline meta-basalts in lower crust depth, leaving behind garnet, amphibole, and plagioclase as the major residual minerals. They are more likely formed in Mongol–Okhotsk oceanic subduction setting.

(d) Lower crustal reworking is pronounced in NE China during Early Cretaceous.

Acknowledgements We are grateful to Wolf-Christian Dullo, Wenjiao Xiao, Kaijun Zhang, and Xiaoping Xia for their constructive and helpful reviews. We would like to thank Jianwei Xiao, Tingting Zhang, Yinchun Su, Yuling Bai, Hongbin Li, and Hongyu Han for their help in field work and zircon U–Pb analyses. This study is financially supported by National Natural Science Foundation of China (41502210) and Geological Survey projects of China Geological Survey (121201 15031301 and DD20160047).

References

Albarede F (1998) The growth of continental crust. Tectonophysics 296(1–2):1–14

Barbarin B (1999) A review of the relationships between granitoid types, their origins and their geodynamic environments. Lithos 46(3):605–626

Barbarin B (2005) Mafic magmatic enclaves and mafic rocks associated with some granitoids of the central Sierra Nevada batholith, California: nature, origin, and relations with the hosts. Lithos 80(1–4):155–177

Barth AP, Wooden JL, Tosdal RM, Morrison J (1995) Crustal contamination in the petrogenesis of a Calc-Alkalic Rock Series—Josephine Mountain Intrusion, California. Geol Soc Am Bull 107(2):201–212

Beard J, Lofgren G (1991) Dehydration melting and water-saturated melting of basaltic and andesitic greenstones and amphibolites at 1, 3, and 6.9 kb. J Petrol 32:365–401

Chappell BW (1999) Aluminium saturation in I- and S-type granites and the characterization of fractionated haplogranites. Lithos 46(3):535–551

Chappell BW, White AJR (1974) Two contrasting granite types. Pac Geol 8:173–174

Chappell BW, White AJR (1992) I-type and S-type granites in the Lachlan Fold Belt. Trans R Soc Edinburgh Earth Sci 83(83):1–26

Chappell BW, Bryant CJ, Wyborn D, White AJR, Williams IS (1998) High- and low-temperature I-type granites. Resour Geol 48(4):225–235

Chappell BW, Bryant CJ, Wyborn D (2012) Peraluminous I-type granites. Lithos 153:142–153

Chen C, Ren YS, Zhao HL, Yang Q, Zou XT (2015) The whole-rock geochemical composition of the Wudaogou group in Eastern Yanbian, NE China-new clues to its relationship with the gold and tungsten mineralization and the evolution of the Paleo-Asian Ocean. Resour Geol 65(3):232–248

Chen H, Xia QK, Ingrin J, Deloule E, Bi Y (2017) Heterogeneous source components of intraplate basalts from NE China induced by the ongoing Pacific slab subduction. Earth Planet Sci Lett 459:208–220

Clemens JD (2003) S-type granitic magmas—petrogenetic issues, models and evidence. Earth Sci Rev 61(1–2):1–18

Cogne JP, Kravchinsky VA, Halim N, Hankard F (2005) Late Jurassic-Early Cretaceous closure of the Mongol-Okhotsk Ocean demonstrated by new Mesozoic palaeomagnetic results from the Trans-Baikal area (SE Siberia). Geophys J Int 163(2):813–832

Collins WJ, Richards SW (2008) Geodynamic significance of S-type granites in circum-Pacific orogens. Geology 36(7):559–562

Collins WJ, Beams SD, White AJR, Chappell BW (1982) Nature and origin of a-type granites with particular reference to Southeastern Australia. Contrib Miner Petrol 80(2):189–200

Cong F, Lin SL, Zou GF, Li ZH, Xie T, Peng ZM, Liang T (2011) Magma mixing of granites at Lianghe: in-situ zircon analysis for trace elements, U–Pb ages and Hf isotopes. Sci China Earth Sci 54(9):1346–1359

Dong Y, Ge WC, Yang H, Zhao GC, Wang QH, Zhang YL, Su L (2014) Geochronology and geochemistry of Early Cretaceous volcanic rocks from the Baiyingaolao Formation in the central Great Xing'an range, NE China, and its tectonic implications. Lithos 205:168–184

Eby GN (1990) The a-type granitoids—a review of their occurrence and chemical characteristics and speculations on their petrogenesis. Lithos 26(1–2):115–134

Eby GN (1992) Chemical subdivision of the a-type granitoids—petrogenetic and tectonic implications. Geology 20(7):641–644

Fritzell EH, Bull AL, Shephard GE (2016) Closure of the Mongol-Okhotsk Ocean: insights from seismic tomography and numerical modelling. Earth Planet Sci Lett 445:1–12

Frost CD, Frost BR (2011) On ferroan (A-type) granitoids: their compositional variability and modes of origin. J Petrol 52(1):39–53

Guo F, Fan WM, Li CW, Gao XF, Miao LC (2009) Early Cretaceous highly positive epsilon(Nd) felsic volcanic rocks from the Hinggan Mountains, NE China: origin and implications for Phanerozoic crustal growth. Int J Earth Sci 98(6):1395–1411

Guo F, Fan WM, Gao XF, Li CW, Miao LC, Zhao LA, Li HX (2010) Sr-Nd-Pb isotope mapping of Mesozoic igneous rocks in NE China Constraints on tectonic framework and Phanerozoic crustal growth. Lithos 120(3–4):563–578

Halim N, Kravchinsky V, Gilder S, Cogne JP, Alexutin M, Sorokin A, Courtillot V, Chen Y (1998) A palaeomagnetic study from the Mongol-Okhotsk region: Rotated Early Cretaceous volcanics and remagnetized Mesozoic sediments. Earth Planet Sci Lett 159:133–145

Hanchar JM, Miller CF (1993) Zircon zonation patterns as revealed by cathodoluminescence and backscattered electron images—implications for interpretation of complex crustal histories. Chem Geol 110(1–3):1–13

Hawkesworth CJ, Kemp AIS (2006) Evolution of the continental crust. Nature 443(7113):811–817

Heilimo E, Elburg MA, Andersen T (2014) Crustal growth and reworking during Lapland–Kola orogeny in northern Fennoscandia: U–Pb and Lu–Hf data from the Nattanen and Litsa-Aragub-type granites. Lithos 205:112–126

Hineab R, Williamscd IS, Chappelle BW, White AJR (1978) Contrasts between I- and S-type granitoids of the Kosciusko Batholith. J Geol Soc Aust 25(3–4):219–234

Huang YL, Wang PJ, Shu P, Zhang YL (2010) Characteristics and formation mechanism of the Cretaceous intermediate and mafic volcanic reservoirs in Songliao Basin, NE China. Acta Petrol Sin 26(1):82–92

IMBGMR (Inner Mongolian Bureau of Geology Mineral Resources) (1991) Regional geology of inner Mongolia. Geological Publishing House, Beijing, pp 1–725 (in Chinese with English abstract)

Jahn BM, Wu FY, Chen B (2000a) Granitoids of the Central Asian Orogenic Belt and continental growth in the Phanerozoic. Trans R Soc Edinburgh Earth Sci 91:181–193

Jahn BM, Wu FY, Chen B (2000b) Massive granitoid generation in Central Asia: Nd isotope evidence and implication for continental growth in the Phanerozoic. Episodes 23(2):82–92

Jahn BM, Capdevila R, Liu DY, Vernon A, Badarch G (2004) Sources of Phanerozoic granitoids in the transect Bayanhongor-Ulaan Baatar, Mongolia: geochemical and Nd isotopic evidence, and implications for Phanerozoic crustal growth. J Asian Earth Sci 23(5):629–653

Jayananda M, Chardon D, Peucat JJ, Capdevila R (2006) 2.61 Ga potassic granites and crustal reworking in the western Dharwar craton, southern India: tectonic, geochronologic and geochemical constraints. Precambr Res 150(1–2):1–26

Ji Z, Ge WC, Wang QH, Yang H, Zhao GC, Bi JH, Dong Y (2016) Petrogenesis of Early Cretaceous volcanic rocks of the Manketouebo Formation in the Wuchagou region, central Great Xing'an range, NE China, and tectonic implications: geochronological, geochemical, and Hf isotopic evidence. Int Geol Rev 58(5):556–573

Kelty TK, Yin A, Dash B, Gehrels GE, Ribeiro AE (2008) Detrital-zircon geochronology of Paleozoic sedimentary rocks in the Hangay–Hentey basin, north-central Mongolia: Implications for the tectonic evolution of the Mongol-Okhotsk Ocean in central Asia. Tectonophysics 451(1–4):290–311

Kemp AIS, Hawkesworth CJ, Foster GL, Paterson BA, Woodhead JD, Hergt JM, Gray CM, Whitehouse MJ (2007a) Magmatic and crustal differentiation history of granitic rocks from Hf–O isotopes in zircon. Science 315(5814):980–983

Kemp AIS, Shimura T, Hawkesworth CJ (2007b) Linking granulites, silicic magmatism, and crustal growth in arcs: ion microprobe (zircon) U–Pb ages from the Hidaka metamorphic belt, Japan. Geology 35(9):807–810

Kemp AIS, Hawkesworth CJ, Collins WJ, Gray CM, Blevin PL, Eimf (2009) Isotopic evidence for rapid continental growth in an extensional accretionary orogen: the Tasmanides, eastern Australia. Earth Planet Sci Lett 284(3–4):455–466

Kravchinsky VA, Cogne JP, Harbert WP, Kuzmin MI (2002) Evolution of the Mongol–Okhotsk Ocean as constrained by new palaeomagnetic data from the Mongol–Okhotsk suture zone, Siberia. Geophys J Int 148:34–57

Le Bas MJ, Le Maitre RW, Streckeisen A, Zanettin B (1986) A chemical classification of volcanic rocks based on the total alkali-silica diagram. J Petrol 27:745–750

Le Maitre RW, Bateman P, Dudek Keller AJ, Lameyre Le Bas MJ, Sabine PA, Schmid R, Sorensen H, Streckeisen A, Wolley AR, Zanetti B (1989) A classification of igneous rocks and glossary of terms. Blackwell, Oxford, p. 193

Li XH, Li ZX, Zhou HW, Liu Y, Kinny PD (2002) U-Pb zircon geochronology, geochemistry and Nd isotopic study of Neoproterozoic bimodal volcanic rocks in the Kangdian Rift of South China: implications for the initial rifting of Rodinia. Precambr Res 113(1–2):135–154

Li SC, Liu ZH, Xu ZY, Li G, Zhang C (2015) Age and tectonic setting of volcanic rocks of the Tamulangou Formation in the Great Xing'an range, NE China. J Asian Earth Sci 113:471–480

Li Y, Xu WL, Wang F, Pei FP, Tang J, Zhao S (2017a) Triassic volcanism along the eastern margin of the Xing'an Massif, NE China: Constraints on the spatial-temporal extent of the Mongol–Okhotsk tectonic regime. Gondwana Res 48:205–223

Li YL, Xu G, Liu HC, Bai LQ, Su YC, Liu XN (2017b) Petrogenesis and tectonic implication of the volcanic rocks in Manitu formation from the Western Great Xing'an range (NE China). Geoscience 31(4):1–15 **(Chinese with English abstract)**

Liu YS, Gao S, Hu ZC, Gao CG, Zong KQ, Wang DB (2010) Continental and oceanic crust recycling-induced melt–peridotite interactions in the trans-north China Orogen: U–Pb dating, Hf isotopes and trace elements in zircons from mantle xenoliths. J Petrol 51(1–2):537–571

Liu RP, Gu XX, Zhang YM, Wang JL, Zheng L, Gao HJ (2015) Zircon U–Pb geochronology and petrogeochemistry of host igneous rocks of the Dong' an gold deposit in Heilongjiang Province, NE China. Acta Petrologica Sinica 31(5):1391–1408

Liu K, Zhang JJ, Wilde SA, Zhou JB, Wang M, Ge MH, Wang JM, Ling YY (2017) Initial subduction of the Paleo-Pacific Oceanic plate in NE China: Constraints from whole-rock geochemistry and zircon U–Pb and Lu–Hf isotopes of the Khanka Lake granitoids. Lithos 274:254–270

Long X, Sun M, Yuan C, Xiao W, Lin S, Wu F, Xia X, Cai K (2007) Detrital zircon age and hf isotopic studies for metasedimentary rocks from the chinese altai: implications for the early paleozoic tectonic evolution of the central Asian orogenic belt. Tectonics 26(5):1–20

Martin H (1999) Adakitic magmas: modern analogues of Archaean granitoids. Lithos 46:411–429

Meng E, Xu WL, Pei FP, Yang DB, Yu Y, Zhang XZ (2010) Detrital-zircon geochronology of Late Paleozoic sedimentary rocks in eastern Heilongjiang Province, NE China: implications for the tectonic evolution of the eastern segment of the Central Asian Orogenic Belt. Tectonophysics 485(1–4):42–51

Pearce JA, Harris NBW, Tindle AG (1984) Trace-Element Discrimination Diagrams for the Tectonic Interpretation of Granitic-Rocks. J Petrol 25(4):956–983

Pei FP, Xu WL, Yang DB, Lu SM, Feng H (2010) Heterogeneity of the lower continental crust beneath southern Jilin Province, NE China: evidence from geochemical and Sr–Nd–Pb isotopic compositions of Early Cretaceous granitoids. Geochimica Et Cosmochimica Acta 74(12):A801-A801

Pei FP, Zhang Y, Wang ZW, Cao HH, Xu WL, Wang ZJ, Wang F, Yang C (2016) Early-Middle Paleozoic subduction-collision history of the south-eastern Central Asian Orogenic Belt: evidence from igneous and metasedimentary rocks of central Jilin Province, NE China. Lithos, 261:164–180

Rapp RP, Watson EB (1995) Dehydration melting of metabasalt at 8–32-Kbar-implications for continental growth and crust-mantle recycling. J Petrol 36(4):891–931

Rapp RP, Shimizu N, Norman MD (2003) Growth of early continental crust by partial melting of eclogite. Nature 425(6958):605–609

Roberts MP, Clemens JD (1993) Origin of high-potassium, calc-alkaline, I-type granitoids. Geology 21(9):825–828

Rudnick RL (1995) Making continental-crust. Nature 378(6557):571–578

Rudnick RL, Fountain DM (1995) Nature and composition of the continental-crust—a lower crustal perspective. Rev Geophys 33(3):267–309

Safonova I (2017) Juvenile versus recycled crust in the Central Asian Orogenic Belt: implications from ocean plate stratigraphy, blueschist belts and intra-oceanic arcs. Gondwana Res 47:6–27

Sawyer EW (1998) Formation and evolution of granite magmas during crustal reworking: the significance of diatexites. J Petrol 39(6):1147–1167

Sengor AMC, Natalin BA, Burtman VS (1993) Evolution of the Altaid Tectonic Collage and Paleozoic Crustal Growth in Eurasia. Nature 364(6435):299–307

Shellnutt JG, Zhou MF (2007) Permian peralkaline, peraluminous and metaluminous A-type granites in the Panxi district, SW China: their relationship to the Emeishan mantle plume. Chem Geol 243(3–4):286–316

Spencer CJ, Cawood PA, Hawkesworth CJ, Raub TD, Prave AR, Roberts NMW (2014) Proterozoic onset of crustal reworking and collisional tectonics: reappraisal of the zircon oxygen isotope record. Geology 42(5):451–454

Sun SS, McDonough WF (1989) Chemical and isotopic systematics of oceanic basalts: implication for mantle composition and process. Geol Soc (Lond), 42(SI):313–345 (Special Publications)

Sun DY, Wu FY, Li HM, Lin Q (2001) Emplacement age of the postorogenic A-type granites in Northwestern Lesser Xing'an ranges, and its relationship to the eastward extension of

Suolushan-Hegenshan-Zhalaite collisional suture zone. Chin Sci Bull 46(5):427–432

Sun DY, Gou J, Ren YS, Fu CL, Wang X, Liu XM (2011) Zircon U-Pb dating and study on geochemistry of volcanic rocks in Manitu Formation from southern Manchuria, Inner Mongolia. Acta Petrol Sin 27(10):3083–3094

Tang GJ, Wang Q, Wyman DA, Li ZX, Zhao ZH, Yang YH (2012) Late Carboniferous high epsilon(Nd)(t)-epsilon(Hf)(t) granitoids, enclaves and dikes in western Junggar, NW China: ridge-subduction-related magmatism and crustal growth. Lithos 140(2012):86–102

Tang J, Xu WL, Wang F, Zhao S, Li Y (2015) Geochronology, geochemistry, and deformation history of Late Jurassic-Early Cretaceous intrusive rocks in the Erguna Massif, NE China: constraints on the late Mesozoic tectonic evolution of the Mongol–Okhotsk orogenic belt. Tectonophysics 658:91–110

Tang J, Xu WL, Wang F, Zhao S, Wang W (2016) Early Mesozoic southward subduction history of the Mongol–Okhotsk oceanic plate: evidence from geochronology and geochemistry of Early Mesozoic intrusive rocks in the Erguna Massif, NE China. Gondwana Res 31:218–240

Thompson AB, Connolly JAD (1995) Melting of the continental-crust—some thermal and petrological constraints on anatexis in continental collision zones and other tectonic settings. J Geophys Res Solid Earth 100(B8):15565–15579

Wang PJ, Ren YG, Shan XL, Sun SB, Wan CB, Bian WH (2002) The Cretaceous volcanic succession around the Songliao Basin, NE China: relationship between volcanism and sedimentation. Geol J 37(2):97–115

Wang F, Zhou XH, Zhang LC, Ying JF, Zhang YT, Wu FY, Zhu RX (2006) Late mesozoic volcanism in the Great Xing'an range (NE China): timing and implications for the dynamic setting of NE Asia. Earth Planet Sci Lett 251(1–2):179–198

Wang YJ, Fan WM, Sun M, Liang XQ, Zhang YH, Peng TP (2007) Geochronological, geochemical and geothermal constraints on petrogenesis of the Indosinian peraluminous granites in the South China Block: a case study in the Hunan Province. Lithos 96(3–4):475–502

Wang PJ, Chen SM, Li WZ, Chen HL, Lang YQ (2010) Chronology, petrology and geochemistry of the Cretaceous crypto-explosive breccia-bearing volcanic rocks: implications for volcanic reservoir and tectonics of the Songliao Basin, NE China. Acta Petrol Sin 26(1):33–46

Wang F, Xu WL, Xu YG, Gao FH, Ge WC (2015a) Late Triassic bimodal igneous rocks in eastern Heilongjiaa Province, NE China: implications for the initiation of subduction of the Paleo-Pacific Plate beneath Eurasia. J Asian Earth Sci 97:406–423

Wang T, Guo L, Zhang L, Yang QD, Zhang JJ, Tong Y, Ye K (2015b) Timing and evolution of Jurassic-Cretaceous granitoid magmatisms in the Mongol-Okhotsk belt and adjacent areas, NE Asia: implications for transition from contractional crustal thickening to extensional thinning and geodynamic settings. J Asian Earth Sci 97:365–392

Wang ZJ, Xu WL, Pei FP, Wang ZW, Li Y, Cao HH (2015c) Geochronology and geochemistry of middle Permian-Middle Triassic intrusive rocks from central-eastern Jilin Province, NE China: constraints on the tectonic evolution of the eastern segment of the Paleo-Asian Ocean. Lithos, 238: 13–25

Wang ZW, Pei FP, Xu WL, Cao HH, Wang ZJ, Zhang Y (2016) Tectonic evolution of the eastern Central Asian Orogenic Belt: evidence from zircon U–Pb–Hf isotopes and geochemistry of early Paleozoic rocks in Yanbian region, NE China. Gondwana Res 38:334–350

Whalen JB, Currie KL, Chappell BW (1987) A-type granites: geochemical characteristics, discrimination and petrogenesis. Contrib Miner Petrol 95:407–419

Winchester JA, Floyd PA (1977) Geochemical discrimination of different magma series and their differentiation products using immobile elements. Chem Geol 20:325–343

Wu FY, Jahn BM, Wilde SA, Lo CH, Yui TF, Lin Q, Ge WC, Sun DY (2003) Highly fractionated I-type granites in NE China (II): isotopic geochemistry and implications for crustal growth in the Phanerozoic. Lithos 67(3–4):191–204

Wu FY, Sun DY, Ge WC, Zhang YB, Grant ML, Wilde SA, Jahn BM (2011) Geochronology of the Phanerozoic granitoids in northeastern China. J Asian Earth Sci 41(1):1–30

Xiao WJ, Windley BF, Hao J, Zhai MG (2003) Accretion leading to collision and the Permian Solonker suture, Inner Mongolia, China: termination of the central Asian orogenic belt. Tectonics, 22(6)

Xiao WJ, Windley BF, Allen MB, Han CM (2013) Paleozoic multiple accretionary and collisional tectonics of the Chinese Tianshan orogenic collage. Gondwana Res 23(4):1316–1341

Xiong FH, Ma CQ, Zhang JY, Liu B, Jiang HA (2014) Reworking of old continental lithosphere: an important crustal evolution mechanism in orogenic belts, as evidenced by Triassic I-type granitoids in the East Kunlun orogen, Northern Tibetan Plateau. J Geol Soc 171(6):847–863

Yang QD, Guo L, Wang T, Zeng T, Zhang L, Tong Y, Shi XJ, Zhang JJ (2014) Geochronology, origin, sources and tectonic settings of Late Mesozoic two-stage granites in the Ganzhuermiao region, central and southern Da Hinggan Range, NE China. Acta Petrol Sin 30(7):1961–1981

Yang YT, Guo ZX, Song CC, Li XB, He S (2015) A short-lived but significant Mongol–Okhotsk collisional orogeny in latest Jurassic-earliest Cretaceous. Gondwana Res 28(3):1096–1116

Yang JH, Peng JT, Zheng YF, Hu RZ, Bi XW, Zhao JH, Huang JC, Zhang BL (2016) Petrogenesis of the Mesozoic Shuikoushan peraluminous I-type granodioritic intrusion in Hunan Province, South China: middle-lower crustal reworking in an extensional tectonic setting. J Asian Earth Sci 123:224–242

Yang DG, Sun DY, Gou J, Hou XG (2017) U-Pb ages of zircons from Mesozoic intrusive rocks in the Yanbian area, Jilin Province, NE China: transition of the Paleo-Asian oceanic regime to the circum-Pacific tectonic regime. J Asian Earth Sci 143:171–190

Yuan HL, Gao S, Liu XM, Li HM, Gunther D, Wu FY (2004) Accurate U-Pb age and trace element determinations of zircon by laser ablation-inductively coupled plasma-mass spectrometry. Geostand Geoanal Res 28(3):353–370

Zeitler PK, Koons PO, Bishop MP, Chamberlain CP, Craw D, Edwards MA, Hamidullah S, Jan MQ, Khan MA, Khattak MUK, Kidd WSF, Mackie RL, Meltzer AS, Park SK, Pecher A, Poage MA, Sarker G, Schneider DA, Seeber L, Shroder JF (2001) Crustal reworking at Nanga Parbat, Pakistan: metamorphic consequences of thermal-mechanical coupling facilitated by erosion. Tectonics 20(5):712–728

Zhang KJ (2014) Genesis of the Late Mesozoic Great Xing'an range Large Igneous Province in eastern central Asia: a Mongol–Okhotsk slab window model. Int Geol Rev 56:1557–1583

Zhang HF, Harris N, Parrish R, Kelley S, Zhang L, Rogers N, Argles T, King J (2004) Causes and consequences of protracted melting of the mid-crust exposed in the North Himalayan antiform. Earth Planet Sci Lett 228(1–2):195–212

Zhang FQ, Chen HL, Yu X, Dong CW, Yang SF, Pang YM, Batt GE (2011) Early Cretaceous volcanism in the northern Songliao Basin, NE China, and its geodynamic implication. Gondwana Res 19(1):163–176

Zhao S, Xu WL, Wang W, Tang J, Zhang YH (2014) Geochronology and geochemistry of Middle-Late ordovician granites and gabbros in the Erguna Region, NE China: implications for the Tectonic Evolution of the Erguna Massif. J Earth Sci 25(5):841–853

Zhou JB, Wilde SA (2013) The crustal accretion history and tectonic evolution of the NE China segment of the Central Asian Orogenic Belt. Gondwana Res 23:1365–1377

Zhou ZB, Pei FP, Wang ZW, Cao HH, Wen-Liang X, Wang ZJ, Zhang Y (2017) Using detrital zircons from late Permian to Triassic sedimentary rocks in the south-eastern Central Asian Orogenic Belt (NE China) to constrain the timing of the final closure of the Paleo-Asian Ocean. J Asian Earth Sci 144:82–109